MGD Application to a Blunt Body in Three-Dimensions

EDISSON SÁVIO DE GÓES MACIEL AND AMILCAR PORTO PIMENTA
IEA- Aeronautical Engineering Division
ITA – Aeronautical Technological Institute
Praça Mal. Eduardo Gomes, 50 – Vila das Acácias – São José dos Campos – SP – 12228-900
BRAZIL
edissonsavio@yahoo.com.br

Abstract: - In this paper, the Euler and Navier-Stokes equations are solved, according to the finite volume formulation and symmetrical structured discretization, applied to the problem of a blunt body in three-dimensions. The work of Gaitonde is the reference one to present the fluid dynamics and Maxwell equations of electromagnetism based on a conservative and finite volume formalisms. The MacCormack and the Jameson and Mavriplis symmetrical schemes are applied to solve the conserved equations. Two types of numerical dissipation models are applied, namely: Mavriplis and Azevedo. A spatially variable time step procedure is employed aiming to accelerate the convergence of the numerical schemes to the steady state solution. The results have proved that, when an induced magnetic field is imposed, an increase in the shock standoff distance is observed, which guarantees a minor increase in the temperature at the blunt body nose.

Key-Words: - Euler and Navier-Stokes equations, Maxwell equations, Magnetogasdynamics formulation, MacCormack algorithm, Jameson and Mavriplis algorithm, Three-dimensions, Finite volumes.

1 Introduction

The effects associated with the interaction of magnetic forces with conducting fluid flows have been profitably employed in several applications related to nuclear and other ([1]) technologies and are known to be essential in the explanation of astrophysical phenomena. In recent years, however, the study of these interactions has received fresh impetus in the effort to solve the problems of high drag and thermal loads encountered in hypersonic flight. The knowledge that electrical and magnetic forces can have profound influence on hypersonic flowfields is not new ([2-3]) – note increased shock-standoff and reduced heat transfer rates in hypersonic flows past blunt bodies under the application of appropriate magnetic fields. The recent interest stems, however, from new revelations of a Russian concept vehicle, known as the AJAX ([4]), which made extensive reference to technologies requiring tight coupling between electromagnetic and fluid dynamic phenomena. A magnetogasdynamic (MGD) generator was proposed ([5]) to extract energy from the incoming air while simultaneously providing more benign flow to the combustion components downstream. The extracted energy could then be employed to increase thrust by MGD pumping of the flow exiting the nozzle or to assist in the generation of a plasma for injection of the body. This latter technique is known to not only reduce drag on the body but also to provide thermal protection ([6]).

In addition to daunting engineering challenges, some of the phenomena supporting the feasibility of an AJAX type vehicle are fraught with controversy (see, for example, [7]). Resolution of these issues will require extensive experimentation as well as simulation. The latter approach requires integration of several disciplines, including fluid dynamics, electromagnetics, chemical kinetics and molecular physics amongst others. This paper describes a recent effort to integrate the first two of these, within the assumptions that characterize ideal and non-ideal magnetogasdynamics.

In this paper, the Euler and Navier-Stokes equations are solved, according to a finite volume formulation and symmetrical structured discretization, applied to the problem of a blunt body in three-dimensions. The work of [8] is the reference one to present the fluid dynamics and Maxwell equations of electromagnetism based on a conservative and finite volume formalisms. The [9] and the [10] symmetrical schemes are applied to solve the conserved equations. Two types of numerical dissipation models are applied, namely: [11-12]. A spatially variable time step procedure is employed aiming to accelerate the convergence of the numerical schemes to the steady state solution. Effective gains in terms of convergence acceleration are observed with this technique ([13-14]).

The results have proved that, when an induced magnetic field is imposed, an increase in the shock standoff distance is observed, which guarantees a

minor increase in the temperature at the blunt body nose (minor armor problems).

2 Formulation to a Flow Submitted to a Magnetic Field

The Navier-Stokes equations to a flow submitted to a magnetic field in a perfect gas formulation are implemented on a finite volume context and three-dimensional space. The Euler equations are obtained by disregarding of the viscous vectors. These equations in integral and conservative forms can be expressed by:

$$\frac{\partial}{\partial t}\int_V Q dV + \int_S \vec{F}\bullet\vec{n} dS = 0 \text{, with:}$$

$$\vec{F} = \left(E_e - E_v\right)\vec{i} + \left(F_e - F_v\right)\vec{j} + \left(G_e - G_v\right)\vec{k} \text{, (1)}$$

where: Q is the vector of conserved variables, V is the computational cell volume, $\vec{F}$ is the complete flux vector, $\vec{n}$ is the unity vector normal to the flux face, S is the flux area, E_e, F_e and G_e are the convective flux vectors or the Euler flux vectors considering the contribution of the magnetic field in the x, y and z directions, respectively, and E_v, F_v and G_v are the viscous flux vectors considering the contribution of the magnetic field in the x, y and z directions, respectively. The unity vectors $\vec{i}$, $\vec{j}$ and $\vec{k}$ define the system of Cartesian coordinates. The vectors Q, E_e, F_e, G_e, E_v, F_v and G_v can be defined, according to [8], as follows:

$$Q = \begin{Bmatrix} \rho \\ \rho u \\ \rho v \\ \rho w \\ \rho Z \\ B_x \\ B_y \\ B_z \end{Bmatrix},\ E_e = \begin{Bmatrix} \rho u \\ \rho u^2 + P - R_b B_x^2/\mu_M \\ \rho uv - R_b B_x B_y/\mu_M \\ \rho uw - R_b B_x B_z/\mu_M \\ (\rho Z + P)u - R_b\left(\vec{V}\bullet\vec{B}/\mu_M\right)B_x \\ 0 \\ uB_y - vB_x \\ uB_z - wB_x \end{Bmatrix}; \quad (2)$$

$$F_e = \begin{Bmatrix} \rho v \\ \rho uv - R_b B_x B_y/\mu_M \\ \rho v^2 + P - R_b B_y^2/\mu_M \\ \rho vw - R_b B_y B_z/\mu_M \\ (\rho Z + P)v - R_b\left(\vec{V}\bullet\vec{B}/\mu_M\right)B_y \\ vB_x - uB_y \\ 0 \\ vB_z - wB_y \end{Bmatrix},$$

$$G_e = \begin{Bmatrix} \rho w \\ \rho uw - R_b B_x B_z/\mu_M \\ \rho vw - R_b B_y B_z/\mu_M \\ \rho w^2 + P - R_b B_z^2/\mu_M \\ (\rho Z + P)w - R_b\left(\vec{V}\bullet\vec{B}/\mu_M\right)B_z \\ wB_x - uB_z \\ wB_y - vB_z \\ 0 \end{Bmatrix}, \quad (3)$$

$$E_v = \begin{Bmatrix} 0 \\ \tau_{xx}/\mathbf{Re} \\ \tau_{xy}/\mathbf{Re} \\ \tau_{xz}/\mathbf{Re} \\ \left(u\tau_{xx} + v\tau_{xy} + w\tau_{xz}\right)/\mathbf{Re} - q_x - q_{J,x} \\ 0 \\ \frac{1}{\mathbf{Re}_\sigma}\frac{1}{\sigma}\left[\frac{\partial}{\partial x}\left(\frac{B_y}{\mu_M}\right) - \frac{\partial}{\partial y}\left(\frac{B_x}{\mu_M}\right)\right] \\ \frac{1}{\mathbf{Re}_\sigma}\frac{1}{\sigma}\left[\frac{\partial}{\partial x}\left(\frac{B_z}{\mu_M}\right) - \frac{\partial}{\partial z}\left(\frac{B_x}{\mu_M}\right)\right] \end{Bmatrix},$$

$$F_v = \begin{Bmatrix} 0 \\ \tau_{xy}/\mathbf{Re} \\ \tau_{yy}/\mathbf{Re} \\ \tau_{yz}/\mathbf{Re} \\ \left(u\tau_{xy} + v\tau_{yy} + w\tau_{yz}\right)/\mathbf{Re} - q_y - q_{J,y} \\ \frac{1}{\mathbf{Re}_\sigma}\frac{1}{\sigma}\left[\frac{\partial}{\partial y}\left(\frac{B_x}{\mu_M}\right) - \frac{\partial}{\partial x}\left(\frac{B_y}{\mu_M}\right)\right] \\ 0 \\ \frac{1}{\mathbf{Re}_\sigma}\frac{1}{\sigma}\left[\frac{\partial}{\partial y}\left(\frac{B_z}{\mu_M}\right) - \frac{\partial}{\partial z}\left(\frac{B_y}{\mu_M}\right)\right] \end{Bmatrix}, \quad (4)$$

$$G_v = \begin{Bmatrix} 0 \\ \tau_{xz}/\mathbf{Re} \\ \tau_{yz}/\mathbf{Re} \\ \tau_{zz}/\mathbf{Re} \\ \left(u\tau_{xz} + v\tau_{yz} + w\tau_{zz}\right)/\mathbf{Re} - q_z - q_{J,z} \\ \frac{1}{\mathbf{Re}_\sigma}\frac{1}{\sigma}\left[\frac{\partial}{\partial z}\left(\frac{B_x}{\mu_M}\right) - \frac{\partial}{\partial x}\left(\frac{B_z}{\mu_M}\right)\right] \\ \frac{1}{\mathbf{Re}_\sigma}\frac{1}{\sigma}\left[\frac{\partial}{\partial z}\left(\frac{B_y}{\mu_M}\right) - \frac{\partial}{\partial y}\left(\frac{B_z}{\mu_M}\right)\right] \\ 0 \end{Bmatrix}, \quad (5)$$

in which: ρ is the fluid density; u, v and w are the Cartesian components of the velocity vector in the x, y and z directions, respectively; Z is the flow total energy considering the contribution of the magnetic field; B_x, B_y and B_z are the Cartesian components of the magnetic field vector active in the x, y and z directions, respectively; P is the pressure term considering the magnetic field effect; R_b is the magnetic force number or the pressure number; μ_M is the mean magnetic permeability, with the value $4\pi x10^{-7}$ T.m/A to the atmospheric air; $\vec{V}$ is the flow velocity vector in Cartesian coordinates; $\vec{B}$ is the magnetic field vector in Cartesian coordinates; the τ's are the components of the viscous stress tensor defined at the Cartesian plane; q_x, q_y and q_z are the components of the Fourier heat flux vector in the x, y and z directions, respectively; $q_{J,x}$, $q_{J,y}$ and $q_{J,z}$ are the components of the Joule heat flux vector in the x, y and z directions, respectively; Re_σ is the magnetic Reynolds number; and σ is the electrical conductivity.

The viscous stresses, in N/m^2, are determined, according to a Newtonian fluid model, by:

$$\tau_{xx} = 2\mu\frac{\partial u}{\partial x} - \frac{2}{3}\mu\left(\frac{\partial u}{\partial x} + \frac{\partial v}{\partial y} + \frac{\partial w}{\partial z}\right), \quad \tau_{xy} = \mu\left(\frac{\partial u}{\partial y} + \frac{\partial v}{\partial x}\right), \quad \tau_{xz} = \mu\left(\frac{\partial u}{\partial z} + \frac{\partial w}{\partial x}\right); \quad (6)$$

$$\tau_{yy} = 2\mu\frac{\partial v}{\partial y} - \frac{2}{3}\mu\left(\frac{\partial u}{\partial x} + \frac{\partial v}{\partial y} + \frac{\partial w}{\partial z}\right), \quad \tau_{yz} = \mu\left(\frac{\partial v}{\partial z} + \frac{\partial w}{\partial y}\right); \quad (7)$$

$$\tau_{zz} = 2\mu\frac{\partial w}{\partial z} - \frac{2}{3}\mu\left(\frac{\partial u}{\partial x} + \frac{\partial v}{\partial y} + \frac{\partial w}{\partial z}\right). \quad (8)$$

where μ is the fluid molecular viscosity. In this work, the empiric formula of Sutherland was employed to the calculation of the molecular viscosity (details in [15]).

Z is the total energy defined by:

$$Z = \frac{p}{(\gamma-1)\rho} + \frac{u^2+v^2+w^2}{2} + R_b\frac{B^2}{2\mu_M\rho} = \frac{p}{(\gamma-1)\rho} + \frac{u^2+v^2+w^2}{2} + R_b\frac{\left(B_x^2+B_y^2+B_z^2\right)}{2\mu_M\rho}. \quad (9)$$

The pressure term is expressed by:

$$P = p + R_b\frac{B^2}{2\mu_M} = p + R_b\frac{\left(B_x^2+B_y^2+B_z^2\right)}{2\mu_M}. \quad (10)$$

The magnetic force number or pressure number is determined by:

$$R_b = \frac{B_\infty^2}{\rho_\infty V_\infty^2\mu_{M,\infty}} = \frac{\left(B_{x,\infty}^2+B_{y,\infty}^2+B_{z,\infty}^2\right)}{\rho_\infty\left(u_\infty^2+v_\infty^2+w_\infty^2\right)\mu_{M,\infty}}. \quad (11)$$

The laminar Reynolds number is defined by:

$$\mathbf{Re} = \frac{\rho_\infty V_\infty L}{\mu_\infty}, \quad (12)$$

in which "∞" represents freestream properties, V_∞ represents the characteristic flow velocity and L is a characteristic length of the studied configuration.

The magnetic Reynolds number is calculated by:

$$\mathbf{Re}_\sigma = LV_\infty\mu_{M,\infty}\sigma_\infty. \quad (13)$$

The components of the Fourier heat flux vector are expressed by:

$$q_x = -\frac{\mu}{(\gamma-1)\mathbf{Pr}\,M_\infty^2\,\mathbf{Re}}\frac{\partial T}{\partial x}, \quad q_y = -\frac{\mu}{(\gamma-1)\mathbf{Pr}\,M_\infty^2\,\mathbf{Re}}\frac{\partial T}{\partial y}; \quad (14)$$

$$q_z = -\frac{\mu}{(\gamma-1)\mathbf{Pr}\,M_\infty^2\,\mathbf{Re}}\frac{\partial T}{\partial z}, \quad (15)$$

with:

$\mathbf{Pr} = \mu_\infty Cp/k$ = 0.72, is the laminar Prandtl number; (16)

$M_\infty = \dfrac{V_\infty}{\sqrt{\gamma p/\rho}}$, is the freestream Mach number; (17)

γ is the ratio of specific heats to a perfect gas, with a value of 1.4 to atmospheric air.

The components of the Joule heat flux vector, which introduces the non-ideal character of the mixed Navier-Stokes / Maxwell equations, are determined by:

$$q_{J,x} = -\frac{R_b}{R_\sigma}\left\{\frac{B_y}{\mu_M\sigma}\left[\frac{\partial}{\partial x}\left(\frac{B_y}{\mu_M}\right)-\frac{\partial}{\partial y}\left(\frac{B_x}{\mu_M}\right)\right]+\frac{B_z}{\mu_M\sigma}\left[\frac{\partial}{\partial x}\left(\frac{B_z}{\mu_M}\right)-\frac{\partial}{\partial z}\left(\frac{B_x}{\mu_M}\right)\right]\right\}; \quad (18)$$

$$q_{J,y} = -\frac{R_b}{R_\sigma}\left\{\frac{B_x}{\mu_M\sigma}\left[\frac{\partial}{\partial y}\left(\frac{B_x}{\mu_M}\right)-\frac{\partial}{\partial x}\left(\frac{B_y}{\mu_M}\right)\right]+\frac{B_z}{\mu_M\sigma}\left[\frac{\partial}{\partial y}\left(\frac{B_z}{\mu_M}\right)-\frac{\partial}{\partial z}\left(\frac{B_y}{\mu_M}\right)\right]\right\}; \quad (19)$$

$$q_{J,z} = -\frac{R_b}{R_\sigma}\left\{\frac{B_x}{\mu_M\sigma}\left[\frac{\partial}{\partial z}\left(\frac{B_x}{\mu_M}\right)-\frac{\partial}{\partial x}\left(\frac{B_z}{\mu_M}\right)\right]+\frac{B_y}{\mu_M\sigma}\left[\frac{\partial}{\partial z}\left(\frac{B_y}{\mu_M}\right)-\frac{\partial}{\partial y}\left(\frac{B_z}{\mu_M}\right)\right]\right\}. \quad (20)$$

3 [9] Structured Algorithm in Three-Dimensions

Employing finite volumes and applying the Green theorem to Eq. (1), one writes:

$$\partial Q_{i,j,k}/\partial t = -1/V_{i,j,k}\int_S\left(\vec{F}\bullet\vec{n}\right)_{i,j,k} dS_{i,j,k}. \quad (21)$$

In the discretization of the surface integral, Eq. (21) can be rewritten as:

$$dQ_{i,j,k}/dt = -1/V_{i,j,k}\left[\left(\vec{F}\bullet\vec{S}\right)_{i,j-1/2,k}+\left(\vec{F}\bullet\vec{S}\right)_{i+1/2,j,k}+\left(\vec{F}\bullet\vec{S}\right)_{i,j+1/2,k}+\left(\vec{F}\bullet\vec{S}\right)_{i-1/2,j,k}+\left(\vec{F}\bullet\vec{S}\right)_{i,j,k-1/2}+\left(\vec{F}\bullet\vec{S}\right)_{i,j,k+1/2}\right]. \quad (22)$$

Discretizing Equation (22) in time employing the explicit Euler method, results in:

$$Q_{i,j,k}^{n+1} = Q_{i,j,k}^{n} - \Delta t_{i,j,k}/V_{i,j,k}\left[(F\cdot S)_{i,j-1/2,k}+(F\cdot S)_{i+1/2,j,k}+(F\cdot S)_{i,j+1/2,k}+(F\cdot S)_{i-1/2,j,k}+(F\cdot S)_{i,j,k-1/2}+(F\cdot S)_{i,j,k+1/2}\right]^n. \quad (23)$$

The time integration is now divided in two steps: one predictor and another corrector. In the predictor step, the convective flux terms are calculated using the properties of the forward cell in relation to the flux interface. The viscous terms are discretized in a symmetrical form. In the corrector step, the properties of the backward cell in relation to the flux interface are employed. The viscous terms are again calculated in a symmetrical form. With this procedure, the scheme is of second order accuracy in space and time. Hence, the [9] algorithm, based on a finite volume formulation, is described as follows:

Predictor step:

$$\begin{aligned}\Delta\overline{Q_{i,j,k}^{n+1}} = &-\Delta t_{i,j,k}/V_{i,j,k}\left\{\left[(E_e)_{i,j,k}-(E_v)_{i,j-1/2,k}\right]S_{x\,i,j-1/2,k}\right.\\
&+\left[(F_e)_{i,j,k}-(F_v)_{i,j-1/2,k}\right]S_{y\,i,j-1/2,k}+\left[(G_e)_{i,j,k}-(G_v)_{i,j-1/2,k}\right]S_{z\,i,j-1/2,k}\\
&+\left[(F_e)_{i+1,j,k}-(F_v)_{i+1/2,j,k}\right]S_{y\,i+1/2,j,k}+\left[(E_e)_{i+1,j,k}-(E_v)_{i+1/2,j,k}\right]S_{x\,i+1/2,j,k}\\
&+\left[(G_e)_{i+1,j,k}-(G_v)_{i+1/2,j,k}\right]S_{z\,i+1/2,j,k}+\left[(E_e)_{i,j+1,k}-(E_v)_{i,j+1/2,k}\right]S_{x\,i,j+1/2,k}\\
&+\left[(F_e)_{i,j+1,k}-(F_v)_{i,j+1/2,k}\right]S_{y\,i,j+1/2,k}+\left[(G_e)_{i,j+1,k}-(G_v)_{i,j+1/2,k}\right]S_{z\,i,j+1/2,k}\\
&+\left[(E_e)_{i,j,k}-(E_v)_{i-1/2,j,k}\right]S_{x\,i-1/2,j,k}+\left[(F_e)_{i,j,k}-(F_v)_{i-1/2,j,k}\right]S_{y\,i-1/2,j,k}\\
&+\left[(G_e)_{i,j,k}-(G_v)_{i-1/2,j,k}\right]S_{z\,i-1/2,j,k}+\left[(E_e)_{i,j,k}-(E_v)_{i,j,k-1/2}\right]S_{x\,i,j,k-1/2}\\
&+\left[(F_e)_{i,j,k}-(F_v)_{i,j,k-1/2}\right]S_{y\,i,j,k-1/2}+\left[(G_e)_{i,j,k}-(G_v)_{i,j,k-1/2}\right]S_{z\,i,j,k-1/2}\\
&+\left[(E_e)_{i,j,k+1}-(E_v)_{i,j,k+1/2}\right]S_{x\,i,j,k+1/2}+\left[(F_e)_{i,j,k+1}-(F_v)_{i,j,k+1/2}\right]S_{y\,i,j,k+1/2}\\
&\left.+\left[(G_e)_{i,j,k+1}-(G_v)_{i,j,k+1/2}\right]S_{z\,i,j,k+1/2}\right\}^n; \quad (24)\end{aligned}$$

$$Q_{i,j,k}^{\overline{n+1}} = Q_{i,j,k}^{n} + \Delta\overline{Q_{i,j,k}^{n+1}}; \quad (25)$$

Corrector step:

$$\begin{aligned}\Delta Q_{i,j,k}^{n+1} = &-\Delta t_{i,j,k}/V_{i,j,k}\left\{\left[(E_e)_{i,j-1,k}-(E_v)_{i,j-1/2,k}\right]S_{x\,i,j-1/2,k}+\right.\\
&+\left[(F_e)_{i,j-1,k}-(F_v)_{i,j-1/2,k}\right]S_{y\,i,j-1/2,k}+\left[(G_e)_{i,j-1,k}-(G_v)_{i,j-1/2,k}\right]S_{z\,i,j-1/2,k}\\
&+\left[(E_e)_{i,j,k}-(E_v)_{i+1/2,j,k}\right]S_{x\,i+1/2,j,k}+\left[(F_e)_{i,j,k}-(F_v)_{i+1/2,j,k}\right]S_{y\,i+1/2,j,k}\\
&+\left[(G_e)_{i,j,k}-(G_v)_{i+1/2,j,k}\right]S_{z\,i+1/2,j,k}+\left[(E_e)_{i,j,k}-(E_v)_{i,j+1/2,k}\right]S_{x\,i,j+1/2,k}\\
&+\left[(F_e)_{i,j,k}-(F_v)_{i,j+1/2,k}\right]S_{y\,i,j+1/2,k}+\left[(G_e)_{i,j,k}-(G_v)_{i,j+1/2,k}\right]S_{z\,i,j+1/2,k}\\
&+\left[(E_e)_{i-1,j,k}-(E_v)_{i-1/2,j,k}\right]S_{x\,i-1/2,j,k}+\left[(F_e)_{i-1,j,k}-(F_v)_{i-1/2,j,k}\right]S_{y\,i-1/2,j,k}\\
&+\left[(G_e)_{i-1,j,k}-(G_v)_{i-1/2,j,k}\right]S_{z\,i-1/2,j,k}+\left[(E_e)_{i,j,k-1}-(E_v)_{i,j,k-1/2}\right]S_{x\,i,j,k-1/2}\\
&+\left[(F_e)_{i,j,k-1}-(F_v)_{i,j,k-1/2}\right]S_{y\,i,j,k-1/2}+\left[(G_e)_{i,j,k-1}-(G_v)_{i,j,k-1/2}\right]S_{z\,i,j,k-1/2}\\
&+\left[(E_e)_{i,j,k}-(E_v)_{i,j,k+1/2}\right]S_{x\,i,j,k+1/2}+\left[(F_e)_{i,j,k}-(F_v)_{i,j,k+1/2}\right]S_{y\,i,j,k+1/2}\\
&\left.+\left[(G_e)_{i,j,k}-(G_v)_{i,j,k+1/2}\right]S_{z\,i,j,k+1/2}\right\}^{\overline{n+1}}; \quad (26)\end{aligned}$$

$$Q_{i,j,k}^{n+1} = 0.5\left(Q_{i,j,k}^{n} + Q_{i,j,k}^{\overline{n+1}} + \Delta Q_{i,j,k}^{n+1}\right). \quad (27)$$

With the intent of guaranteeing numerical stability to the [9] scheme, in its three-dimensional version, an artificial dissipation operator of second and fourth differences ([16-17]) is subtracted from the flux terms of the right side (RHS, "Right Hand Side") in the corrector step, aiming to eliminate instabilities originated from shock waves and due to the field stability. The operator is of the following type: $D_{i,j,k} = d^{(2)}_{i,j,k} - d^{(4)}_{i,j,k}$, defined in section **4.1**.

4 [10] Structured Algorithm in Three-Dimensions

Equation (1) can be rewritten following a structured spatial discretization context ([10, 18]) as:

$$d\left(V_{i,j,k}Q_{i,j,k}\right)/dt + C(Q_{i,j,k}) = 0, \qquad (28)$$

where:

$$\begin{aligned}C(Q_{i,j,k}) = {} & \left\{0.5\left[(E_e)_{i,j,k} + (E_e)_{i,j-1,k}\right] - (E_v)_{i,j-1/2,k}\right\}S_{x_{i,j-1/2,k}} + \\ & + \left\{0.5\left[(F_e)_{i,j,k} + (F_e)_{i,j-1,k}\right] - (F_v)_{i,j-1/2,k}\right\}S_{y_{i,j-1/2,k}} + \left\{0.5\left[(G_e)_{i,j,k} + (G_e)_{i,j-1,k}\right] - (G_v)_{i,j-1/2,k}\right\}S_{z_{i,j-1/2,k}} \\ & + \left\{0.5\left[(E_e)_{i,j,k} + (E_e)_{i+1,j,k}\right] - (E_v)_{i+1/2,j,k}\right\}S_{x_{i+1/2,j,k}} + \left\{0.5\left[(F_e)_{i,j,k} + (F_e)_{i+1,j,k}\right] - (F_v)_{i+1/2,j,k}\right\}S_{y_{i+1/2,j,k}} \\ & + \left\{0.5\left[(G_e)_{i,j,k} + (G_e)_{i+1,j,k}\right] - (G_v)_{i+1/2,j,k}\right\}S_{z_{i+1/2,j,k}} + \left\{0.5\left[(E_e)_{i,j,k} + (E_e)_{i,j+1,k}\right] - (E_v)_{i,j+1/2,k}\right\}S_{x_{i,j+1/2,k}} \\ & + \left\{0.5\left[(F_e)_{i,j,k} + (F_e)_{i,j+1,k}\right] - (F_v)_{i,j+1/2,k}\right\}S_{y_{i,j+1/2,k}} + \left\{0.5\left[(G_e)_{i,j,k} + (G_e)_{i,j+1,k}\right] - (G_v)_{i,j+1/2,k}\right\}S_{z_{i,j+1/2,k}} \\ & + \left\{0.5\left[(E_e)_{i,j,k} + (E_e)_{i-1,j,k}\right] - (E_v)_{i-1/2,j,k}\right\}S_{x_{i-1/2,j,k}} + \left\{0.5\left[(F_e)_{i,j,k} + (F_e)_{i-1,j,k}\right] - (F_v)_{i-1/2,j,k}\right\}S_{y_{i-1/2,j,k}} \\ & + \left\{0.5\left[(G_e)_{i,j,k} + (G_e)_{i-1,j,k}\right] - (G_v)_{i-1/2,j,k}\right\}S_{z_{i-1/2,j,k}} + \left\{0.5\left[(E_e)_{i,j,k} + (E_e)_{i,j,k-1}\right] - (E_v)_{i,j,k-1/2}\right\}S_{x_{i,j,k-1/2}} \\ & + \left\{0.5\left[(F_e)_{i,j,k} + (F_e)_{i,j,k-1}\right] - (F_v)_{i,j,k-1/2}\right\}S_{y_{i,j,k-1/2}} + \left\{0.5\left[(G_e)_{i,j,k} + (G_e)_{i,j,k-1}\right] - (G_v)_{i,j,k-1/2}\right\}S_{z_{i,j,k-1/2}} \\ & + \left\{0.5\left[(E_e)_{i,j,k} + (E_e)_{i,j,k+1}\right] - (E_v)_{i,j,k+1/2}\right\}S_{x_{i,j,k+1/2}} + \left\{0.5\left[(F_e)_{i,j,k} + (F_e)_{i,j,k+1}\right] - (F_v)_{i,j,k+1/2}\right\}S_{y_{i,j,k+1/2}} \\ & + \left\{0.5\left[(G_e)_{i,j,k} + (G_e)_{i,j,k+1}\right] - (G_v)_{i,j,k+1/2}\right\}S_{z_{i,j,k+/2}} \qquad (29)\end{aligned}$$

is the approximation to the flux integral of Eq. (1). In this work, one adopts that, for example, the flux vector E_e at the flux interface (i,j-1/2,k) is obtained by the arithmetical average between the E_e vector calculated at the cell (i,j,k) and the E_e vector calculated at the cell (i,j-1,k). The viscous flux vectors are calculated in a symmetrical form as demonstrated in section 5.

The spatial discretization proposed by the authors is equivalent to a symmetrical scheme with second order accuracy, on a finite difference context. The introduction of an artificial dissipation operator "D" is necessary to guarantee the scheme numerical stability in presence of, for example, uncoupled odd/even solutions and non-linear stabilities, as shock waves. Equation (28) can, so, be rewritten as:

$$d\left(V_{i,j,k}Q_{i,j,k}\right)/dt + \left[C(Q_{i,j,k}) - D(Q_{i,j,k})\right] = 0. \qquad (30)$$

The time integration is performed by a hybrid Runge-Kutta method of five stages, with second order accuracy, and can be represented in general form as:

$$\begin{aligned}Q^{(0)}_{i,j,k} &= Q^{(n)}_{i,j,k} \\ Q^{(l)}_{i,j,k} &= Q^{(0)}_{i,j,k} - \alpha_l \Delta t_{i,j,k} \big/ V_{i,j,k}\left[C\left(Q^{(l-1)}_{i,j,k}\right) - D\left(Q^{(m)}_{i,j,k}\right)\right], \qquad (31) \\ Q^{(n+1)}_{i,j,k} &= Q^{(l)}_{i,j,k}\end{aligned}$$

where: l = 1,...,5; m = 0 until 4; $\alpha_1 = 1/4$, $\alpha_2 = 1/6$, $\alpha_3 = 3/8$, $\alpha_4 = 1/2$ and $\alpha_5 = 1$. [10] suggest that the artificial dissipation operator should be evaluated only in the first two stages as the Euler equations were solved (m = 0, l = 1 and m = 1, l = 2). [19] suggest that the artificial dissipation operator should be evaluated in alternated stages as the Navier-Stokes equations were solved (m = 0, l = 1, m = 2, l = 3 and m = 4, l = 5). These procedures aim CPU time economy and also better damping of the numerical instabilities originated from the discretization based on the hyperbolic characteristics of the Euler equations and the hyperbolic/parabolic characteristics of the Navier-Stokes equations.

4.1 Artificial dissipation operator

The artificial dissipation operator implemented in the [9-10] schemes has the following structure:

$$D\left(Q_{i,j,k}\right) = d^{(2)}\left(Q_{i,j,k}\right) - d^{(4)}\left(Q_{i,j,k}\right), \qquad (32)$$

where:

$$\begin{aligned}d^{(2)}\left(Q_{i,j,k}\right) = {} & 0.5\varepsilon^{(2)}_{i,j-1/2,k}\left(A_{i,j,k} + A_{i,j-1,k}\right)\left(Q_{i,j-1,k} - Q_{i,j,k}\right) \\ & + 0.5\varepsilon^{(2)}_{i+1/2,j,k}\left(A_{i,j,k} + A_{i+1,j,k}\right)\left(Q_{i+1,j,k} - Q_{i,j,k}\right) + 0.5\varepsilon^{(2)}_{i,j+1/2,k}\left(A_{i,j,k} + A_{i,j+1,k}\right)\left(Q_{i,j+1,k} - Q_{i,j,k}\right) \\ & + 0.5\varepsilon^{(2)}_{i-1/2,j,k}\left(A_{i,j,k} + A_{i-1,j,k}\right)\left(Q_{i-1,j,k} - Q_{i,j,k}\right) + 0.5\varepsilon^{(2)}_{i,j,k-1/2}\left(A_{i,j,k} + A_{i,j,k-1}\right)\left(Q_{i,j,k-1} - Q_{i,j,k}\right) \\ & + 0.5\varepsilon^{(2)}_{i,j,k+1/2}\left(A_{i,j,k} + A_{i,j,k+1}\right)\left(Q_{i,j,k+1} - Q_{i,j,k}\right), \qquad (33)\end{aligned}$$

named undivided Laplacian operator, is responsible by the numerical stability in the presence of shock waves; and

$$\begin{aligned}d^{(4)}\left(Q_{i,j,k}\right) = {} & 0.5\varepsilon^{(4)}_{i,j-1/2,k}\left(A_{i,j,k} + A_{i,j-1,k}\right)\left(\nabla^2 Q_{i,j-1,k} - \nabla^2 Q_{i,j,k}\right) \\ & + 0.5\varepsilon^{(4)}_{i+1/2,j,k}\left(A_{i,j,k} + A_{i+1,j,k}\right)\left(\nabla^2 Q_{i+1,j,k} - \nabla^2 Q_{i,j,k}\right) + 0.5\varepsilon^{(4)}_{i,j+1/2,k}\left(A_{i,j,k} + A_{i,j+1,k}\right)\left(\nabla^2 Q_{i,j+1,k} - \nabla^2 Q_{i,j,k}\right) \\ & + 0.5\varepsilon^{(4)}_{i-1/2,j,k}\left(A_{i,j,k} + A_{i-1,j,k}\right)\left(\nabla^2 Q_{i-1,j,k} - \nabla^2 Q_{i,j,k}\right) + 0.5\varepsilon^{(4)}_{i,j,k-1/2}\left(A_{i,j,k} + A_{i,j,k-1}\right)\left(\nabla^2 Q_{i,j,k-1} - \nabla^2 Q_{i,j,k}\right) \\ & + 0.5\varepsilon^{(4)}_{i,j,k+1/2}\left(A_{i,j,k} + A_{i,j,k+1}\right)\left(\nabla^2 Q_{i,j,k+1} - \nabla^2 Q_{i,j,k}\right), \qquad (34)\end{aligned}$$

named bi-harmonic operator, is responsible by the background stability (for example: instabilities originated from uncoupled odd/even solutions). In this last term,

$$\nabla^2 Q_{i,j,k} = \left(Q_{i,j-1,k} - Q_{i,j,k}\right) + \left(Q_{i+1,j,k} - Q_{i,j,k}\right) + \left(Q_{i,j+1,k} - Q_{i,j,k}\right) + \left(Q_{i-1,j,k} - Q_{i,j,k}\right) + \\ + \left(Q_{i,j,k-1} - Q_{i,j,k}\right) + \left(Q_{i,j,k+1} - Q_{i,j,k}\right). \quad (35)$$

In the $d^{(4)}$ operator, $\nabla^2 Q_{i,j,k}$ is extrapolated from the value of the real neighbor cell every time that it represent a ghost cell. The ε terms are defined, for instance, as:

$$\varepsilon^{(2)}_{i,j-1/2,k} = K^{(2)} MAX\left(\nu_{i,j,k}, \nu_{i,j-1,k}\right), \\ \varepsilon^{(4)}_{i,j-1/2,k} = MAX\left[0, \left(K^{(4)} - \varepsilon^{(2)}_{i,j-1/2,k}\right)\right], \quad (36)$$

with:

$$\nu_{i,j,k} = \left(\left|p_{i,j-1,k} - p_{i,j,k}\right| + \left|p_{i+1,j,k} - p_{i,j,k}\right| + \left|p_{i,j+1,k} - p_{i,j,k}\right| + \left|p_{i-1,j,k} - p_{i,j,k}\right| + \left|p_{i,j,k-1} - p_{i,j,k}\right| + \left|p_{i,j,k+1} - p_{i,j,k}\right|\right) / \\ \left(p_{i,j-1,k} + p_{i+1,j,k} + p_{i,j+1,k} + p_{i-1,j,k} + p_{i,j,k-1} + p_{i,j,k+1} + 6p_{i,j,k}\right) \quad (37)$$

representing a pressure sensor employed to identify regions of elevated gradients. The $K^{(2)}$ and $K^{(4)}$ constants has typical values of 1/4 and 3/256, respectively. Every time that a neighbor cell represents a ghost cell, one assumes, for example, that $\nu_{ghost} = \nu_{i,j,k}$. The $A_{i,j}$ terms can be defined according to two models implemented in this work: (a) [11] and (b) [12]. In the first case, the $A_{i,j}$ terms are contributions from the maximum normal eigenvalue of the Euler equations integrated along each cell face. Hence, they are defined as follows:

(a) [11] model:

$$A_{i,j,k} = \left[\left|u^1_{int} S_{x_{i,j-1/2,k}} + v^1_{int} S_{y_{i,j-1/2,k}} + w^1_{int} S_{z_{i,j-1/2,k}}\right| + a^1_{int}\left(S^2_{x_{i,,j-1/2,k}} + S^2_{y_{i,j-1/2,k}} + S^2_{z_{i,j-1/2,k}}\right)^{0.5}\right] + \\ + \left[\left|u^2_{int} S_{x_{i+1/2,j,k}} + v^2_{int} S_{y_{i+1/2,j,k}} + w^2_{int} S_{z_{i+1/2,j,k}}\right| + a^2_{int}\left(S^2_{x_{i+1/2,j,k}} + S^2_{y_{i+1/2,j,k}} + S^2_{z_{i+1/2,j,k}}\right)^{0.5}\right] \\ + \left[\left|u^3_{int} S_{x_{i,j+1/2,k}} + v^3_{int} S_{y_{i,j+1/2,k}} + w^3_{int} S_{z_{i,j+1/2,k}}\right| + a^3_{int}\left(S^2_{x_{i,j+1/2,k}} + S^2_{y_{i,j+1/2,k}} + S^2_{z_{i,j+1/2,k}}\right)^{0.5}\right] \\ + \left[\left|u^4_{int} S_{x_{i-1/2,j,k}} + v^4_{int} S_{y_{i-1/2,j,k}} + w^4_{int} S_{z_{i-1/2,j,k}}\right| + a^4_{int}\left(S^2_{x_{i-1/2,j,k}} + S^2_{y_{i-1/2,j,k}} + S^2_{z_{i-1/2,,j,k}}\right)^{0.5}\right] \\ + \left[\left|u^5_{int} S_{x_{i,j,k-1/2}} + v^5_{int} S_{y_{i,j,k-1/2}} + w^5_{int} S_{z_{i,j,k-1/2}}\right| + a^5_{int}\left(S^2_{x_{i,j,k-1/2}} + S^2_{y_{i,j,k-1/2}} + S^2_{z_{i,j,k-1/2}}\right)^{0.5}\right] \\ + \left[\left|u^6_{int} S_{x_{i,j,k+1/2}} + v^6_{int} S_{y_{i,j,k+1/2}} + w^6_{int} S_{z_{i,j,k+1/2}}\right| + a^6_{int}\left(S^2_{x_{i,j,k+1/2}} + S^2_{y_{i,j,k+1/2}} + S^2_{z_{i,j,k+1/2}}\right)^{0.5}\right]. \quad (38)$$

where "a" represents the sound speed and, for instance, $u^1_{int} = 0.5\left(u_{i,j,k} + u_{i,j-1,k}\right)$.

(b) [12] model:

$$A_{i,j,k} = V_{i,j,k} / \Delta t_{i,j,k}, \quad (39)$$

which represents a scaling factor, according to structured meshes, with the desired behavior to the artificial dissipation term: (i) bigger control volumes result in bigger value to the dissipation term; (ii) smaller time steps also result in bigger values to the scaling term.

5 Calculation of the Viscous Gradients

The viscous vectors at the flux interface are obtained by the arithmetical average between the primitive variables at the right and left states of the flux interface, as also the arithmetical average of the primitive variable gradients, also considering the right and left states of the flux interface. The gradients of the primitive variables present in the viscous flux vectors are calculated employing the Green theorem, which considers that the gradient of a primitive variable is constant in the volume and that the volume integral which defines this gradient is replaced by a surface integral. This methodology to calculation of the viscous gradients is based on the work of [20]. As an example, one has to $\partial u/\partial x$:

$$\frac{\partial u}{\partial x} = \frac{1}{V}\int_V \frac{\partial u}{\partial x} dV = \frac{1}{V}\int_S u\left(\vec{n} \bullet d\vec{S}\right) = \frac{1}{V}\int_{S_x} u dS_x \cong \frac{1}{V_{i,j,k}}\left[0.5\left(u_{i,j,k} + u_{i,j-1,k}\right)S_{x_{i,j-1/2,k}} + \right. \\ 0.5\left(u_{i,j,k} + u_{i+1,j,k}\right)S_{x_{i+1/2,j,k}} + 0.5\left(u_{i,j,k} + u_{i,j+1,k}\right)S_{x_{i,j+1/2,k}} + 0.5\left(u_{i,j,k} + u_{i-1,j,k}\right)S_{x_{i-1/2,j,k}} \\ \left. + 0.5\left(u_{i,j,k} + u_{i,j,k-1}\right)S_{x_{i,j,k-1/2}} + 0.5\left(u_{i,j,k} + u_{i,j,k+1}\right)S_{x_{i,j,k+1/2}}\right]. \quad (40)$$

The dimensionless employed in the Euler and Navier-Stokes equations, the boundary conditions, the geometry configuration and the employed meshes are presented in [21].

6 Results

Tests were performed in three microcomputers: one with processor INTEL CELERON, 1.5GHz of clock and 1.0GBytes of RAM (notebook), the second with processor AMD SEMPRON (tm) 2600+, 1.83GHz of clock and 512 Mbytes of RAM (desktop), and the third one with processor INTEL CELERON 2.13GHz of clock and 1.0GBytes of RAM (notebook). As the interest of this work is steady state problems, one needs to define a

criterion which guarantees that such condition was reached. The criterion adopted in this work was to consider a reduction of no minimal three (3) orders in the magnitude of the maximum residual in the domain, a typical criterion in the CFD community. The residual to each cell was defined as the numerical value obtained from the discretized conservation equations. As there are eight (8) conservation equations to each cell, the maximum value obtained from these equations is defined as the residual of this cell. Thus, this residual is compared with the residual of the other cells, calculated of the same way, to define the maximum residual in the domain. In the simulations, the attack angle, α, was set equal to zero.

6.1 Initial conditions

The initial conditions to the standard simulation of the studied algorithms are presented in Tab. 1. This is a benchmark case to the flow submitted to a magnetic field normal to the symmetry line of the blunt body configuration. The Reynolds number was calculated from the data of [22].

Table 1. 3D initial conditions.

Property	Value
M_∞	10.6
$B_{y,\infty}$	0.15 T
μ_M	1.2566×10^{-6} T.m/A
σ_∞	1,000 ohm/m
Altitude	40,000 m
Pr	0.72
L (2D)	2.0 m
Re_∞ (2D)	1.6806×10^6

6.2. Numerical results

6.2.1. Results with the [9] scheme to inviscid flow in three-dimensions

Figures 1 and 2 present the pressure contours calculated at the computational domain to the inviscid gas flow submitted to a magnetic field. Figures 1 and 2 exhibit the solutions obtained with the [9] scheme employing the artificial dissipation models of [12] and [11], respectively. The pressure field obtained by the [9] scheme employing the dissipation model of [11] is more intense than that obtained with the dissipation model of [12]. Good symmetry properties are observed in both solutions.

Figures 3 and 4 show the Mach number contours calculated at the computational domain by the [9] scheme employing the artificial dissipation models of [12] and of [11], respectively. The Mach number field obtained by the [9] scheme employing the dissipation model of [11] is more intense. Good symmetry properties are observed in both solutions. The shock wave develops naturally, passing from a normal shock at the symmetry line to oblique shock waves along the body and finishing in a Mach wave, far from the geometry.

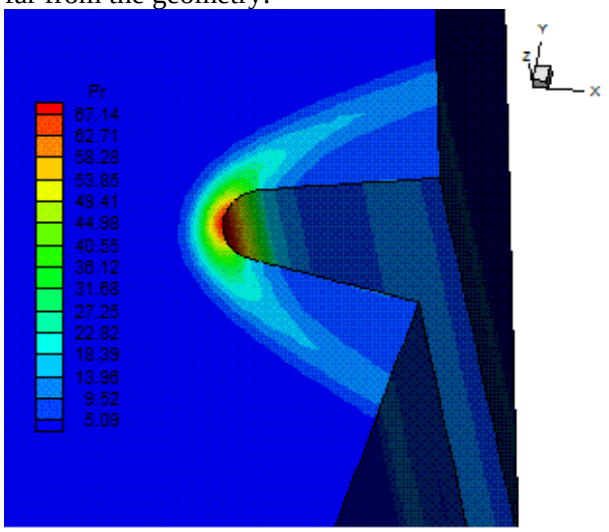

Figure 1 : Pressure Contours ([9]/[12]).

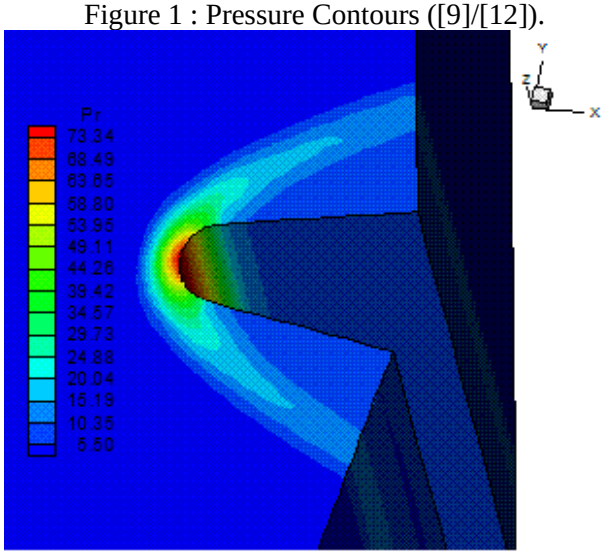

Figure 2 : Pressure Contours ([9]/[11]).

Figures 5 and 6 present the translational / rotational temperature distributions calculated at the computational domain. The [9] scheme with the artificial dissipation model of [12] predicts a more severe temperature field.

Figures 7 and 8 exhibit the contours of the B_x component of the magnetic field vector determined at the calculation domain. As can be observed, the B_x component is negative at the geometry lower surface and positive at the geometry upper surface, indicating that the magnetic field performs a curve around the geometry. The solution presented by the [9] scheme with the dissipation model of [11] is

quantitatively more symmetrical than the respective one obtained with the dissipation model of [12], although the latter presents a more intense B_x component field.

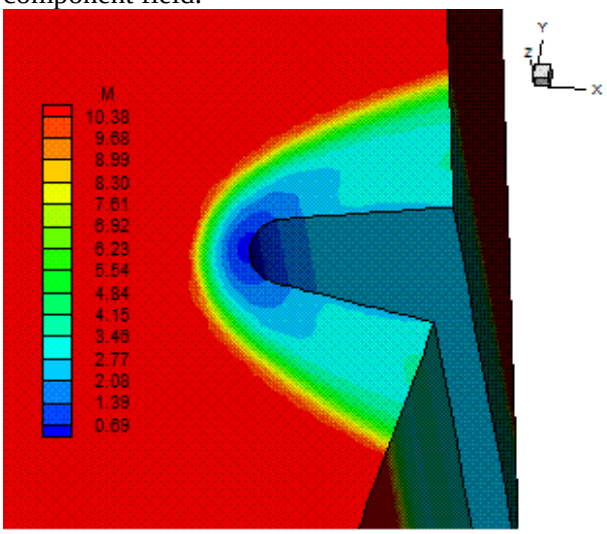

Figure 3 : Mach Number Contours ([9]/[12]).

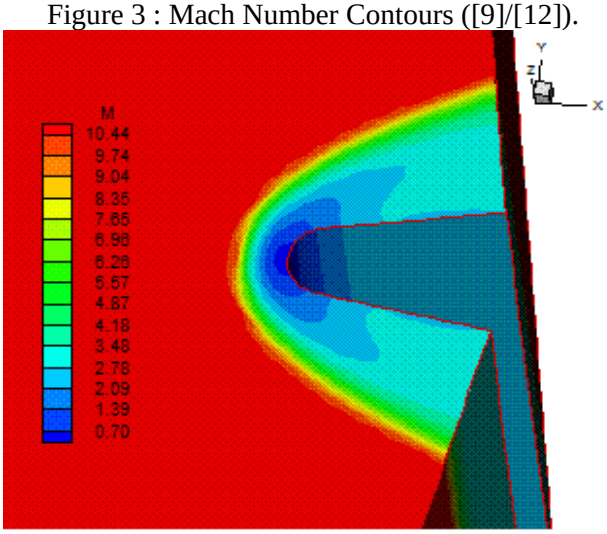

Figure 4 : Mach number Contours ([9]/[11]).

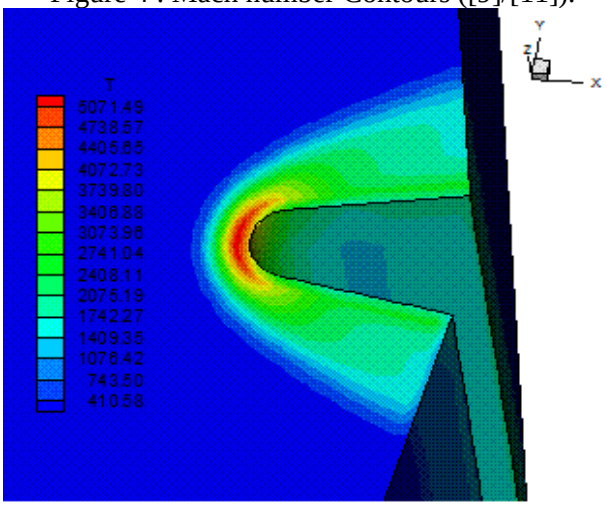

Figure 5 : Temperature Contours ([9]/[12]).

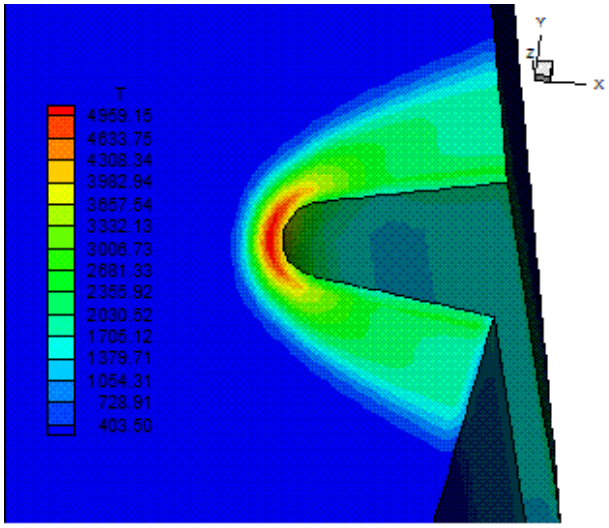

Figure 6 : Temperature Contours ([9]/[11]).

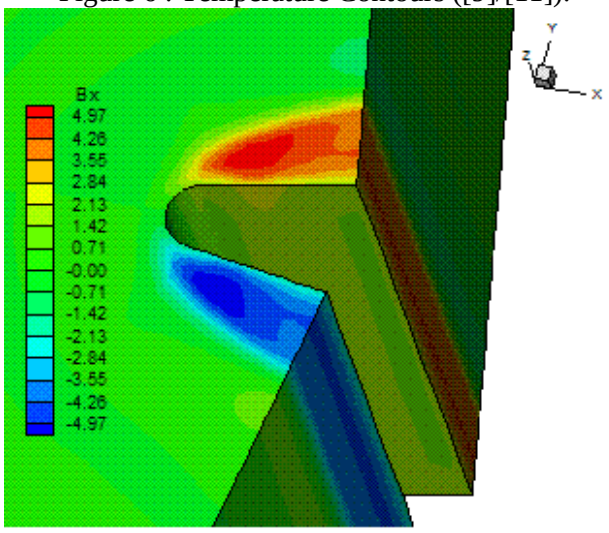

Figure 7 : B_x Component of Magnetic Field ([9]/[12]).

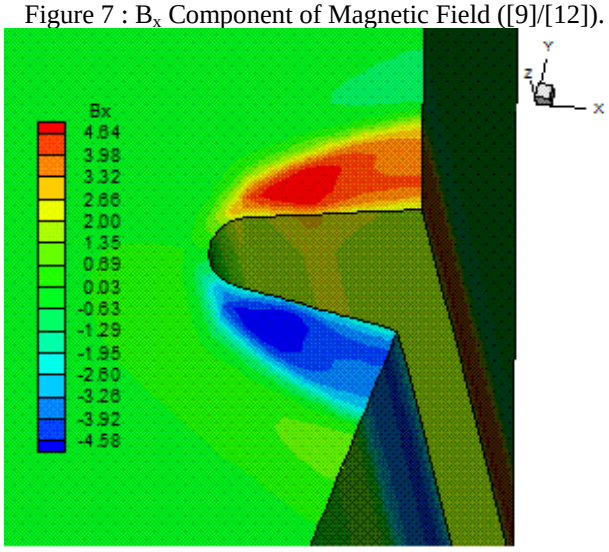

Figure 8 : B_x Component of Magnetic Field ([9]/[11]).

Figures 9 and 10 exhibit the magnetic vector field with induction lines to highlight the satisfied initial condition far ahead of the configuration and the distortion in these lines close to the blunt body. As can be observed, the magnetic induction lines are

initially attracted to the magnetic field imposed at the blunt body walls and, close to the body, suffer distortion, getting round the configuration.

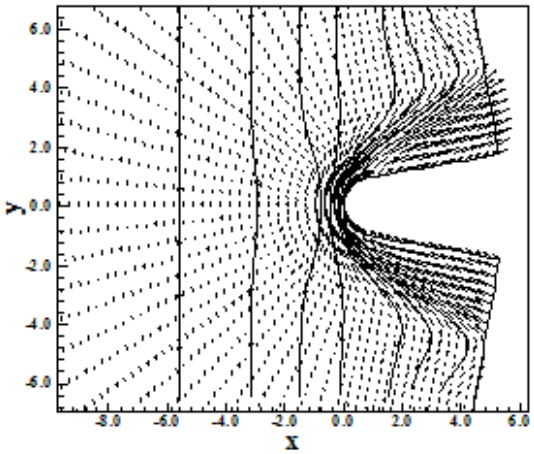

Figure 9 : Magnetic Field and Induction Lines ([9]/[12]).

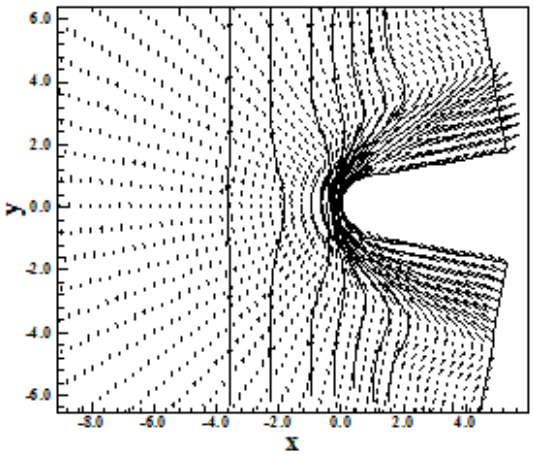

Figure 10 : Magnetic Field and Induction Lines ([9]/[11]).

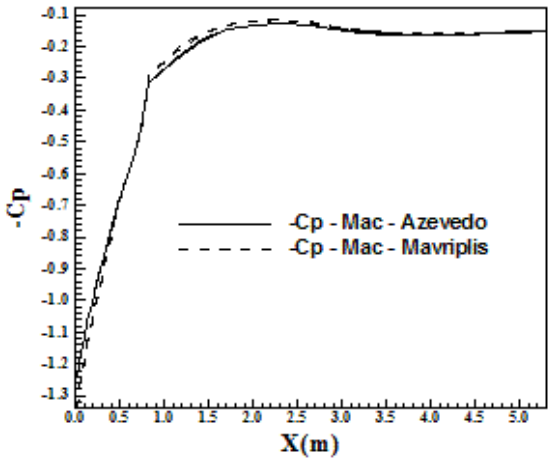

Figure 11 : -Cp Distributions.

Figure 11 shows the –Cp distributions along the blunt body wall. As can be seen, the shock captured by the [9] scheme employing the dissipation model of [11] is more severe than that obtained with the dissipation model of [12], presenting a Cp peak at the configuration nose bigger. Figure 12 presents the distribution of the translational / rotational temperature along the configuration symmetry line or configuration stagnation line. As can be noted, the dissipation models predict different shock wave positions. [12] model predicts the shock wave at 1.60m ahead of the blunt body nose, while the [11] model predicts the shock wave at 1.30m ahead of the blunt body nose.

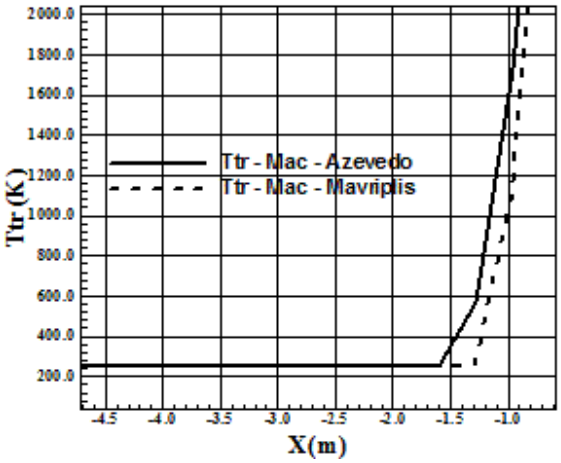

Figure 12 : Shock Position by the Temperature profile.

6.2.2 Results with the [9] scheme to viscous flow in three-dimensions

Figures 13 and 14 exhibit the pressure contours calculated at the computational domain. The pressure field obtained by the [9] scheme employing the dissipation model of [12] is more intense than that obtained with the dissipation model of [11], with a behavior opposed to that observed in the inviscid solution. Good symmetry properties are observed in both solutions.

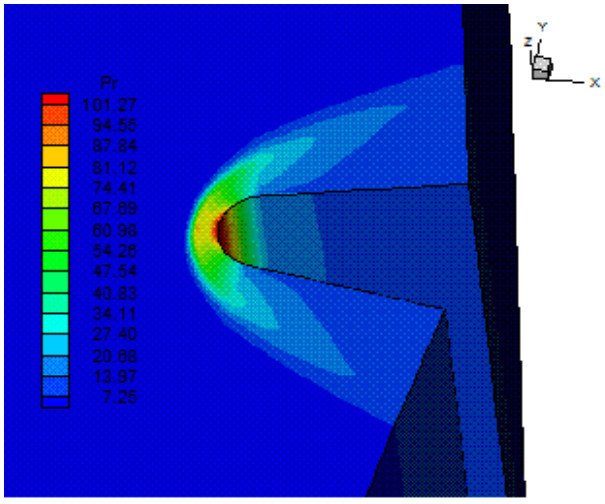

Figure 13 : Pressure Contours ([9]/[12]).

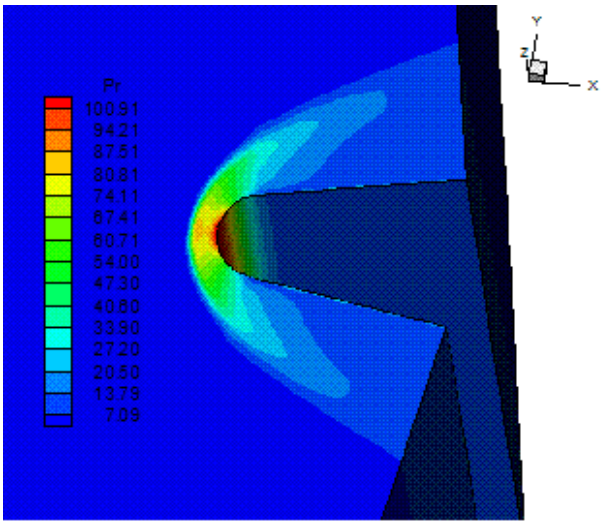

Figure 14 : Pressure Contours ([9]/[11]).

Figures 15 and 16 show the Mach number contours calculated at the computational domain by the [9] scheme employing the artificial dissipation models of [12] and of [11], respectively. The Mach number field obtained by the [9] scheme employing the dissipation model of [11] is more intense. It is important to note that both solutions present pre-shock oscillation problems, being more critical those observed in the solution with [11] model. Good symmetry properties are observed in both solutions.

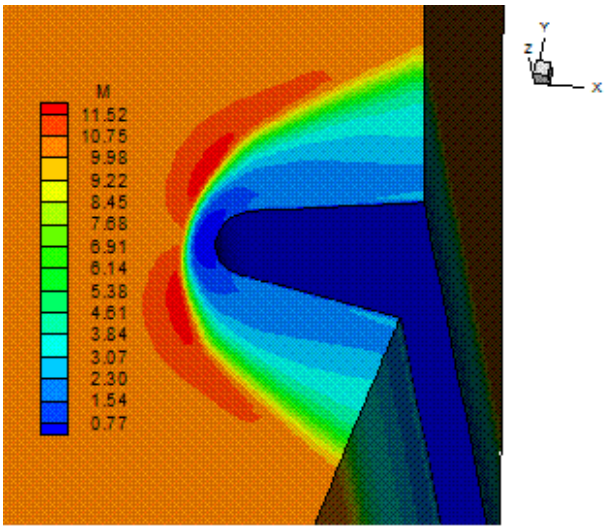

Figure 15 : Mach Number Contours ([9]/[12]).

Figures 17 and 18 present the translational / rotational temperature distributions calculated at the computational domain. The [9] scheme with the artificial dissipation model of [11] predicts a more severe temperature field. This temperature field is much more severe than that obtained by the inviscid solution. The temperature peak occurs along the rectilinear walls, by the development of the wall heating due to the consideration of viscous effects.

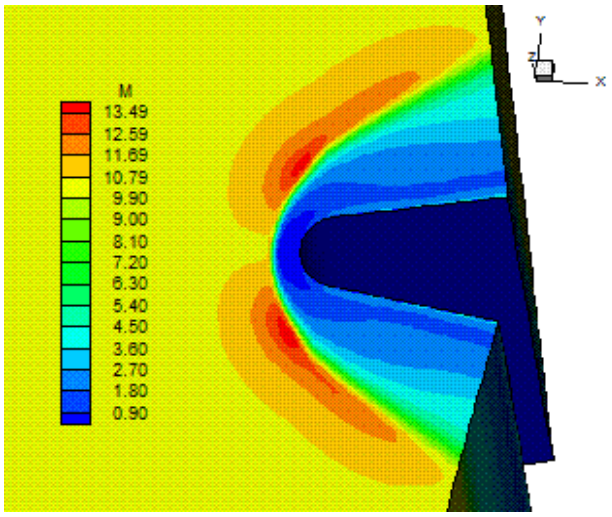

Figure 16 : Mach Number Contours ([9]/[11]).

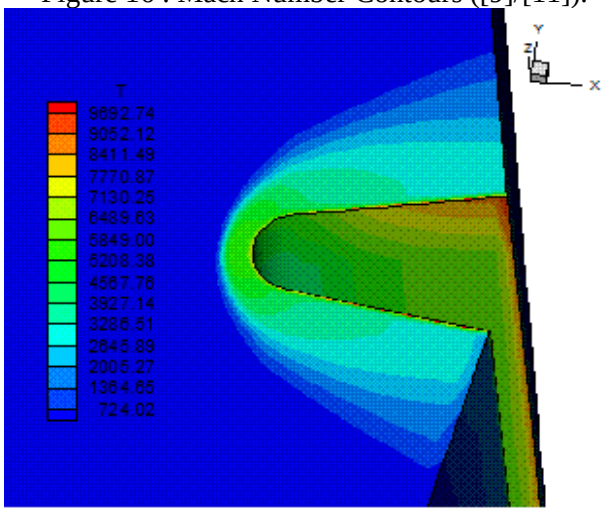

Figure 17 : Temperature Contours ([9]/[12]).

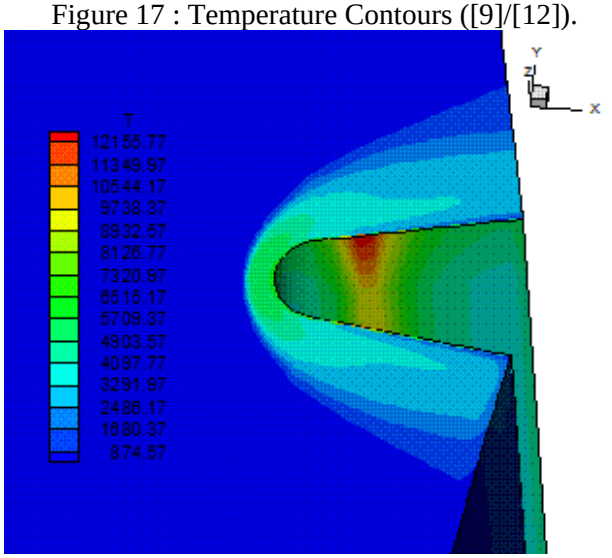

Figure 18 : Temperature contours ([9]/[11]).

Figures 19 and 20 exhibit the contours of the B_x component of the magnetic field vector determined at the calculation domain. As can be observed, the B_x component is negative at the geometry lower surface and positive at the geometry upper surface, indicating that the magnetic field performs a curve

around the geometry. The solutions presented by the [9] scheme with the dissipation models of [12] and of [11] have meaningful numerical non-symmetry. The dissipation model of [11] presents a B_x field more intense.

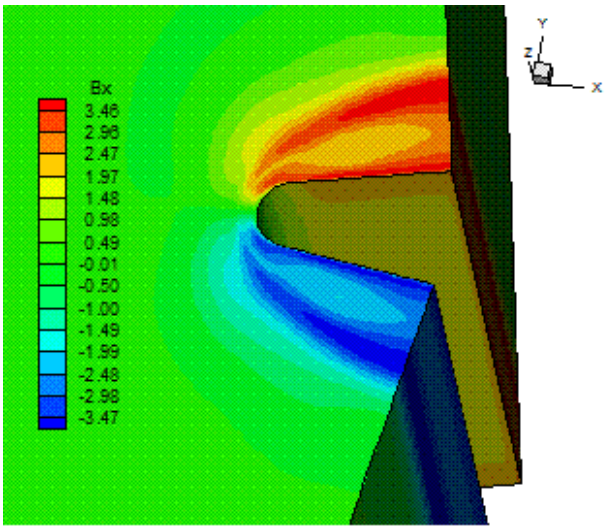

Figure 19 : B_x Component of Magnetic Field ([9]/[11]).

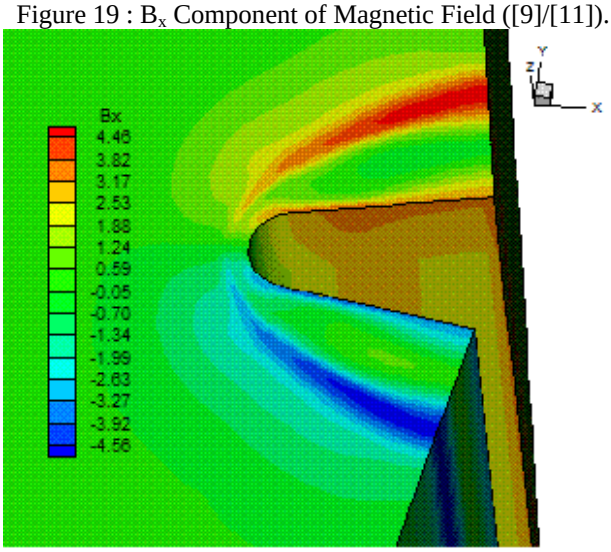

Figure 20 : B_x Component of Magnetic Field ([9]/[11]).

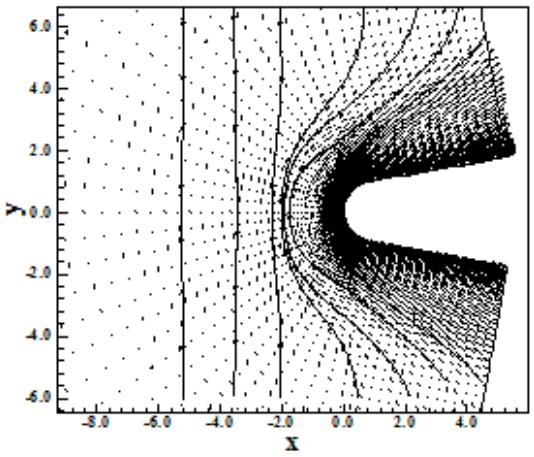

Figure 21 : Magnetic Field and Induction Lines ([9]/[12]).

Figures 21 and 22 exhibit the magnetic vector field with induction lines to highlight the satisfied initial condition far ahead of the configuration and the distortion in these lines close to the blunt body. As can be observed, the magnetic induction lines are initially attracted to the magnetic field imposed at the blunt body walls and, close to the body, suffer distortion, getting round the configuration.

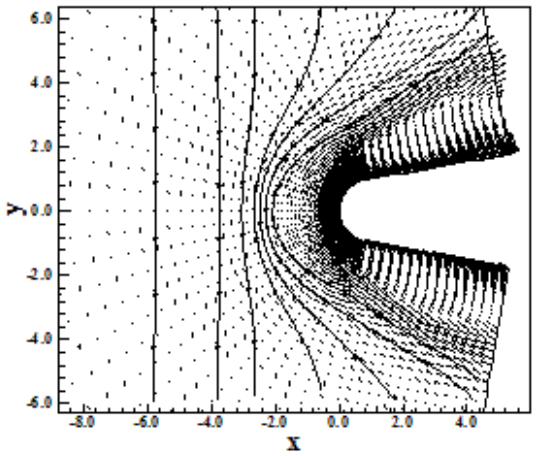

Figure 22 : Magnetic Field and Induction Lines ([9]/{11]).

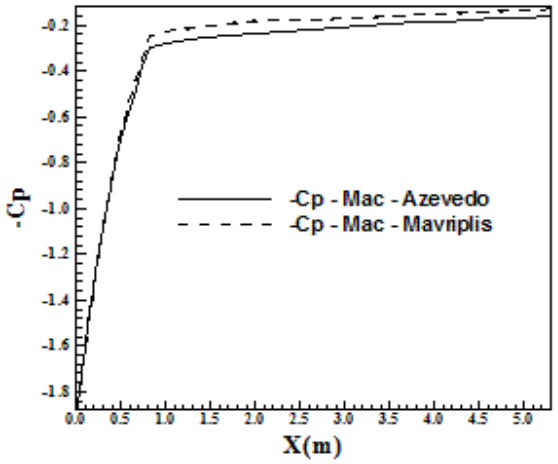

Figure 23 : -Cp Distributions.

Figure 23 shows the –Cp distributions along the blunt body wall. As can be seen, the shock captured by the [9] scheme employing the dissipation model of [11] is more severe than that obtained with the dissipation model of [12], presenting bigger Cp variation between the configuration nose and the configuration rectilinear walls. Figure 24 presents the distribution of the translational / rotational temperature along the configuration symmetry line or configuration stagnation line. As can be noted, the dissipation models predict different shock wave positions. The [12] model predicts the shock wave at 0.90m ahead of the blunt body nose, while the [11]

model predicts the shock wave at 0.80m ahead of the blunt body nose.

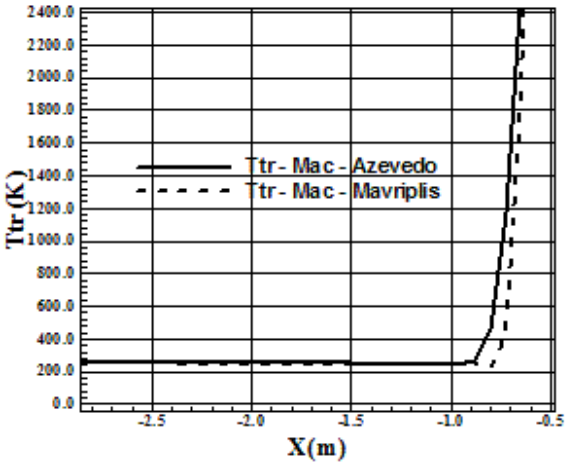

Figure 24 : Shock Position by the Temperature Profile.

6.2.3 Results with the [10] scheme to inviscid flow in three-dimensions

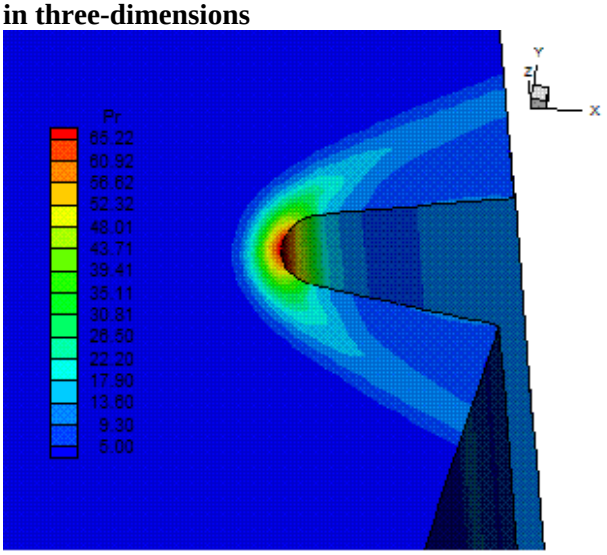

Figure 25 : Pressure Contours ([10]/[12]).

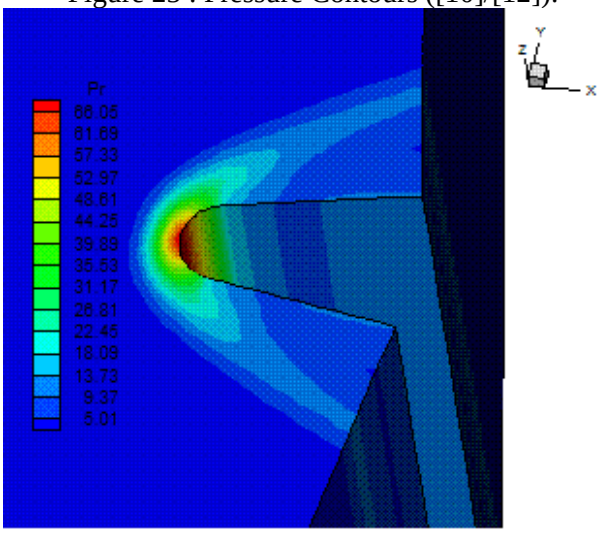

Figure 26 : Pressure Contours ([10]/[11]).

Figure 25 and 26 present the pressure contours calculated at the computational domain. The pressure contours obtained by the [10] scheme employing the dissipation model of [11] is more intense than that obtained with the dissipation model of [12]. Good symmetry properties are observed in both solutions.

Figures 27 and 28 exhibit the Mach number contours calculated at the computational domain by the [10] scheme employing the artificial dissipation models of [12] and of [11], respectively. The Mach number field obtained by the [10] scheme employing the dissipation model of [11] is more intense. Good symmetry properties are observed in both solutions. The shock wave develops naturally, passing from a normal shock (frontal) to a Mach wave, through oblique shock waves.

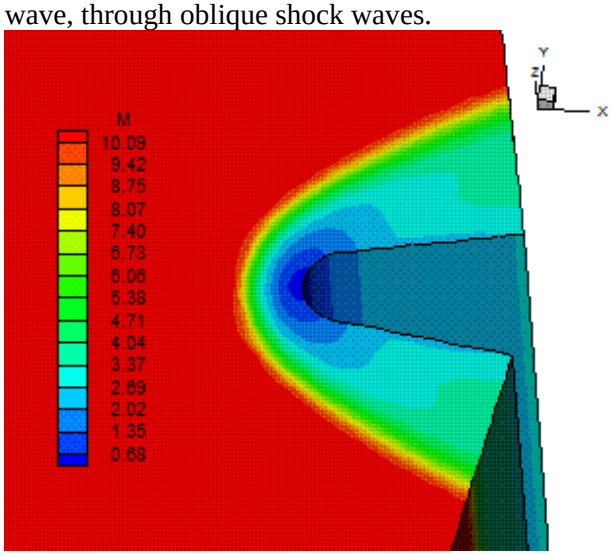

Figure 27 : Mach Number Contours ([10]/[12]).

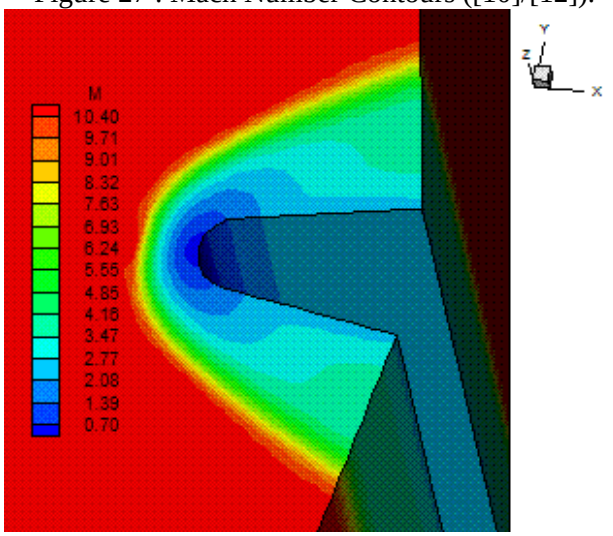

Figure 28 : Mach Number Contours ([10]/[11]).

Figures 29 and 30 show the translational / rotational temperature distributions calculated at the computational domain. The [10] scheme with the artificial dissipation model of [12] predicts a more

severe temperature field. This field is, however, inferior in intensity to the respective one calculated by the [9] scheme, as seen in Fig. 5.

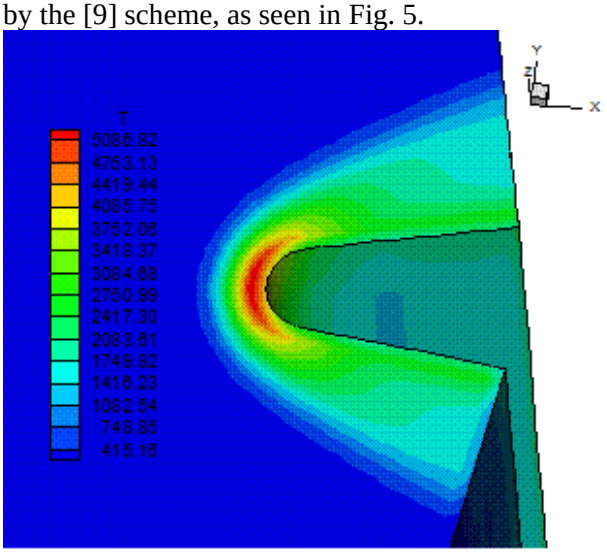

Figure 29 : Temperature Contours ([10]/[12]).

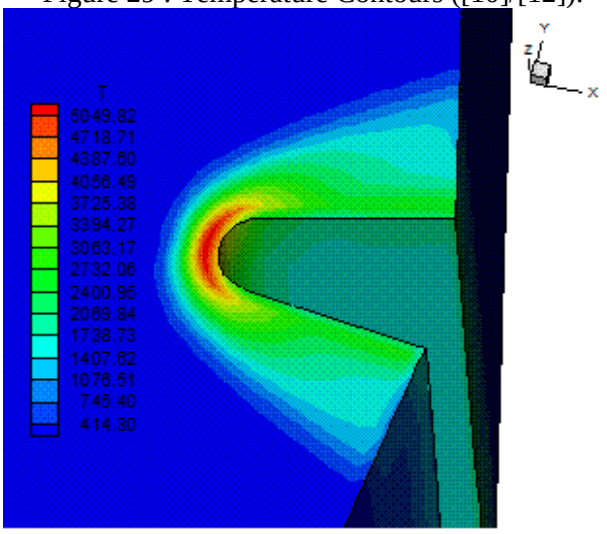

Figure 30 : Temperature Contours ([10]/[11]).

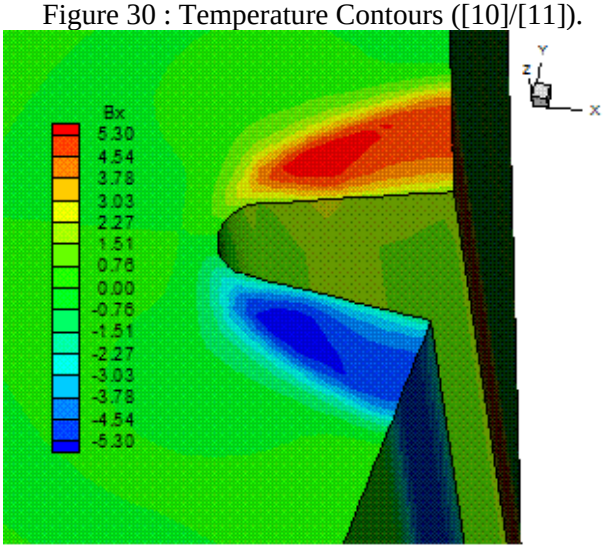

Figure 31 : B_x Component of Magnetic Field ([10]/[12]).

Figures 31 and 32 exhibit the contours of the B_x component of the magnetic field vector determined at the calculation domain. As can be observed, the B_x component is negative at the geometry lower surface and positive at the geometry upper surface, indicating that the magnetic field performs a curve around the geometry, equally observed in the solutions with the [9] scheme. The solutions presented by the [10] scheme with the dissipation models of [12] and of [11] have good symmetry properties. The latter solution presents a B_x field more intense.

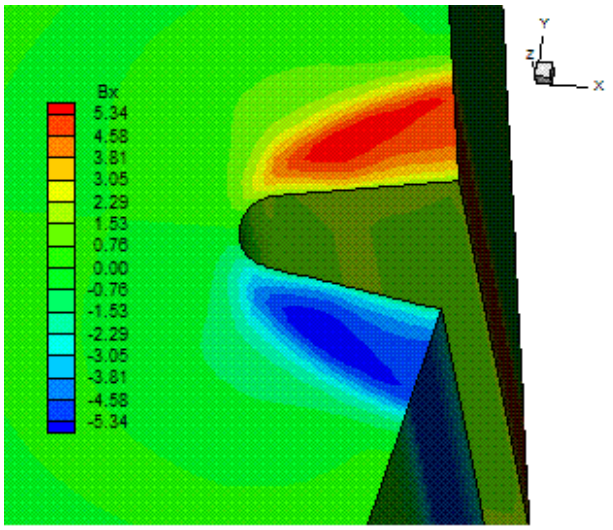

Figure 32 : B_x Component of Magnetic Field ([10]/[11]).

Figures 33 and 34 exhibit the magnetic vector field with induction lines to highlight the satisfied initial condition far ahead of the configuration and the distortion in these lines close to the blunt body. As can be observed, the magnetic induction lines are initially attracted to the magnetic field imposed at the blunt body walls and, close to the body, suffer distortion, getting round the configuration. The same behavior was observed in the inviscid solutions obtained with the [9] scheme.

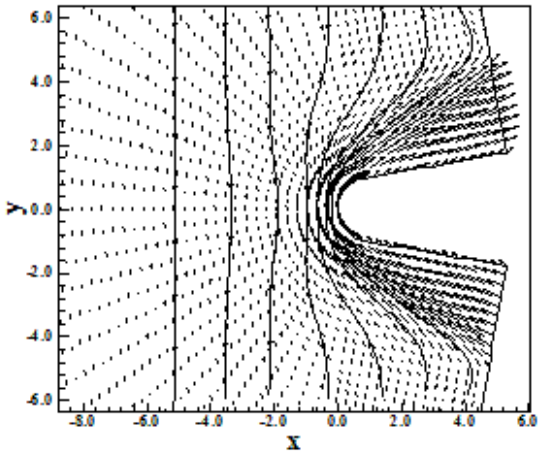

Figure 33 : Magnetic Field and Induction Lines ([10]/[12]).

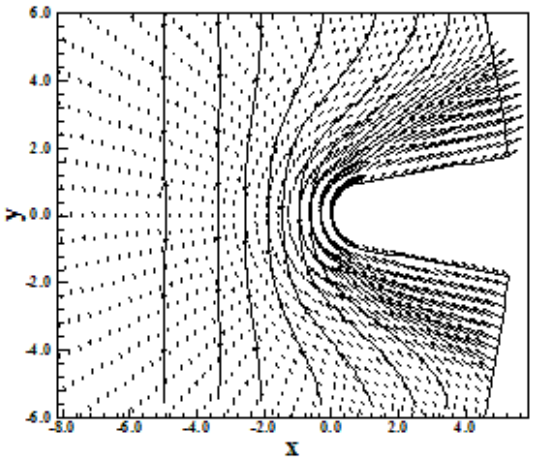

Figure 34 : Magnetic Field and Induction Lines ([10]/[11]).

Figure 35 shows the –Cp distributions along the blunt body wall. As can be seen, the shock captured by the [10] scheme employing both dissipation models present the same intensity.

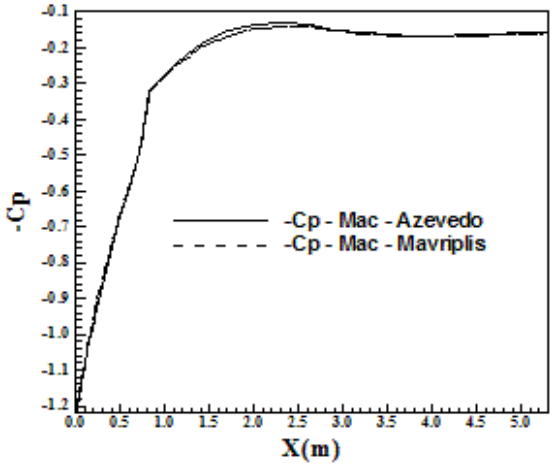

Figure 35 : -Cp Distributions.

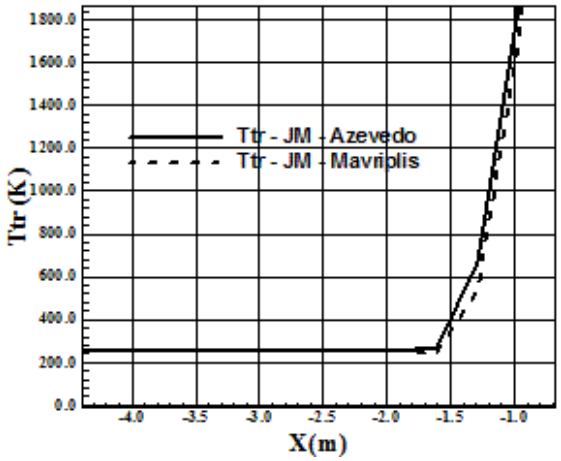

Figure 36 : Shock Position by the Temperature Profile.

Figure 36 presents the distribution of the translational / rotational temperature along the configuration symmetry line or configuration stagnation line. As can be noted, the dissipation models predict approximately the same shock wave positions. The [11-12] models predict the shock wave at 1.60m ahead of the blunt body nose.

6.2.4 Results with the [10] scheme to viscous flow in three-dimensions

Figure 37 and 38 present the pressure contours calculated at the computational domain. The pressure contours obtained by the [10] scheme employing the dissipation model of [12] is more intense than that obtained with the dissipation model of [11], opposed to the behavior observed in the inviscid solution. Good symmetry properties are observed in both solutions. This field is also more intense than the respective one obtained with the [9] scheme employing the same dissipation model.

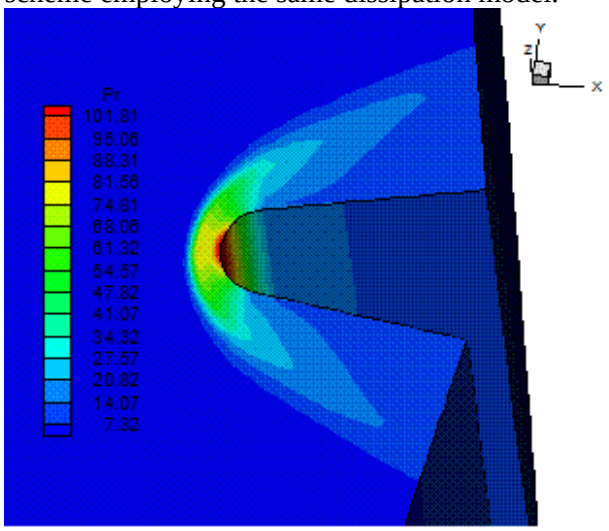

Figure 37 : Pressure Contours ([10]/[12]).

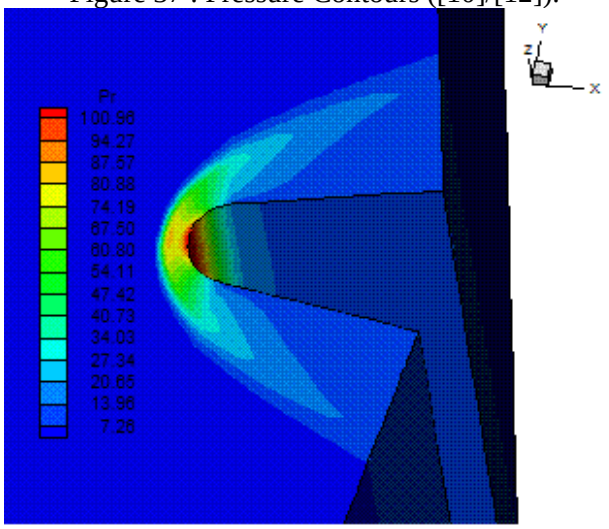

Figure 38 : Pressure Contours (JM/M).

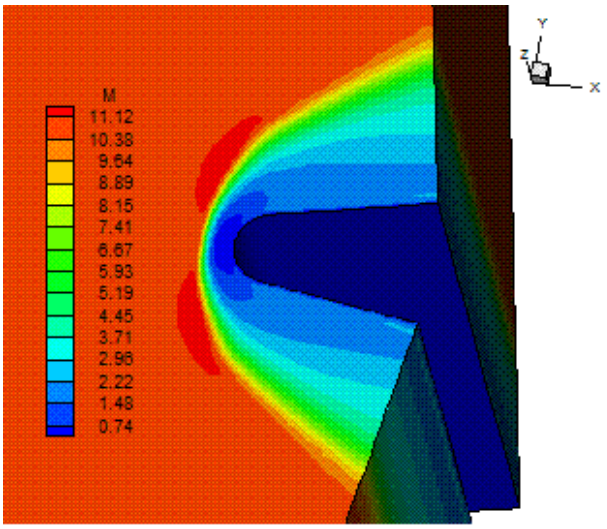

Figure 39 : Mach Number Contours ([10]/[12]).

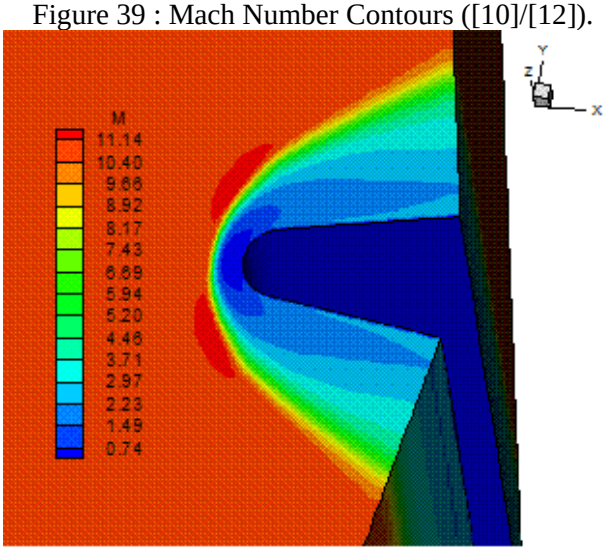

Figure 40 : Mach Number Contours ([10]/[11]).

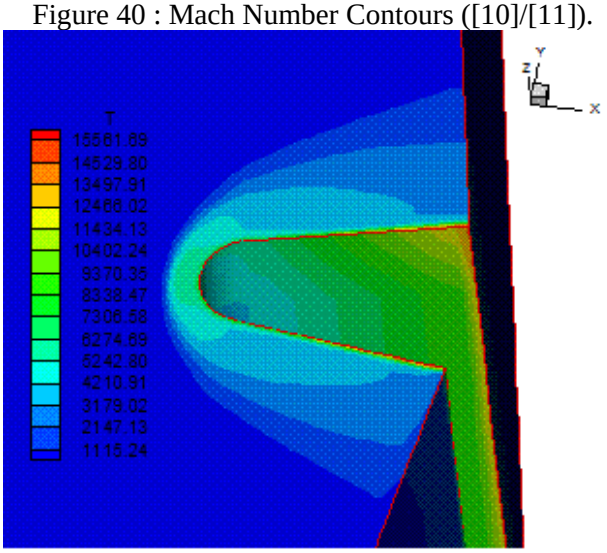

Figure 41 : Temperature Contours ([10]/[12]).

Figures 39 and 40 exhibit the Mach number contours calculated at the computational domain by the [10] scheme employing the artificial dissipation models of [12] and of [11], respectively. The Mach number field obtained by the [10] scheme employing the dissipation model of [11] is more intense. It is important to note that both solutions present problems of pre-shock oscillations, being the [11] model solution as quantitatively more critical. Good symmetry properties are observed in both solutions.

Figures 41 and 42 show the translational / rotational temperature distributions calculated at the computational domain. The [10] scheme with the artificial dissipation model of [12] predicts a more severe temperature field, much more severe than the respective one obtained with the [9] scheme. This field is much more severe than that obtained with the inviscid solution of the present scheme. The temperature peak occurs along the rectilinear walls, by the development of the heating acting in these walls, due to the consideration of viscous effects.

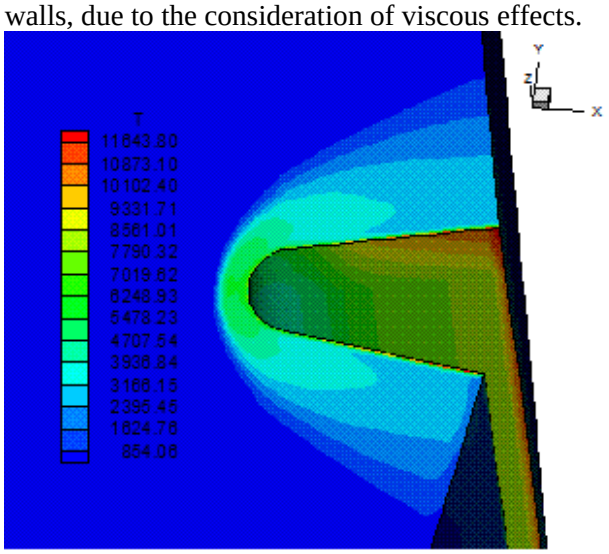

Figure 42 : Temperature Contours ([10]/[11]).

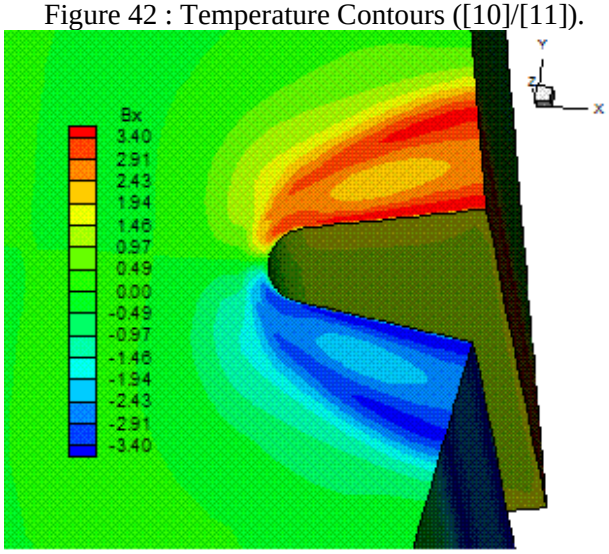

Figure 43 : B_x Component of Magnetic Field ([10]/[12]).

Figures 43 and 44 exhibit the contours of the B_x component of the magnetic field vector determined at the calculation domain. As can be observed, the B_x component is negative at the geometry lower

surface and positive at the geometry upper surface, indicating that the magnetic field performs a curve around the geometry. The solutions presented by the [10] scheme with the dissipation models of [12] and of [11] have meaningful symmetry properties. The dissipation model of [11] presents a B_x field more intense.

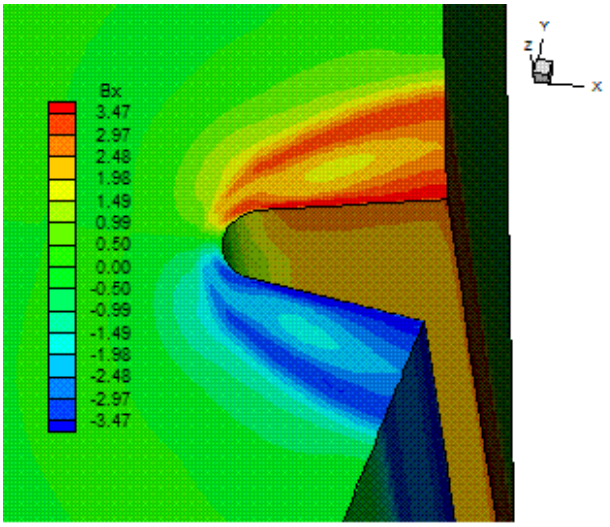

Figure 44 : B_x Component of Magnetic Field ([10]/[11]).

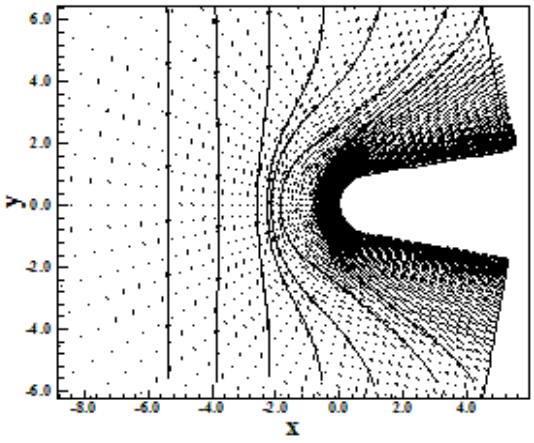

Figure 45 : Magnetic Field and Induction Lines ([10]/[12]).

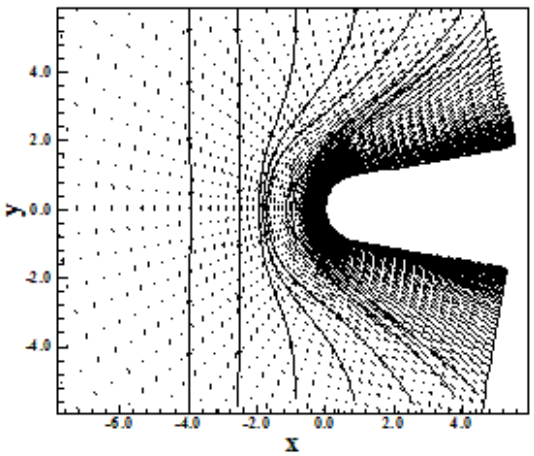

Figure 46 : Magnetic Field and Induction Lines ([10]/[11]).

Figures 45 and 46 exhibit the magnetic vector field with induction lines to highlight the satisfied initial condition far ahead of the configuration and the distortion in these lines close to the blunt body. As can be observed, the magnetic induction lines are initially attracted to the magnetic field imposed at the blunt body walls and, close to the body, suffer distortion, getting round the configuration. The same behavior was observed in the respective solutions obtained with the [9] scheme.

Figure 47 shows the –Cp distributions along the blunt body wall. As can be seen, the shock captured by the [10] scheme employing the [11] dissipation model is more severe than that obtained with the [12] dissipation model, presenting bigger variation in the Cp value between the nose and the rectilinear walls of the blunt body.

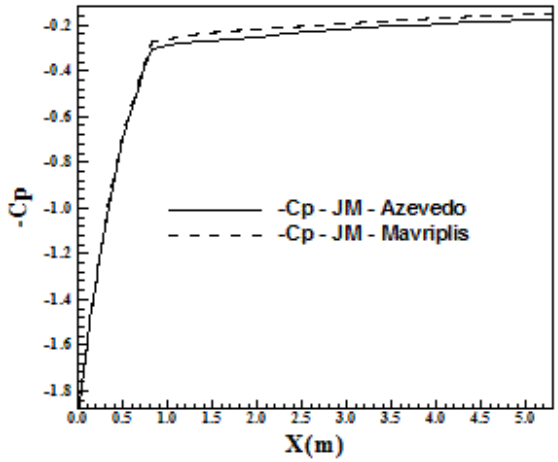

Figure 47 : -Cp Distributions.

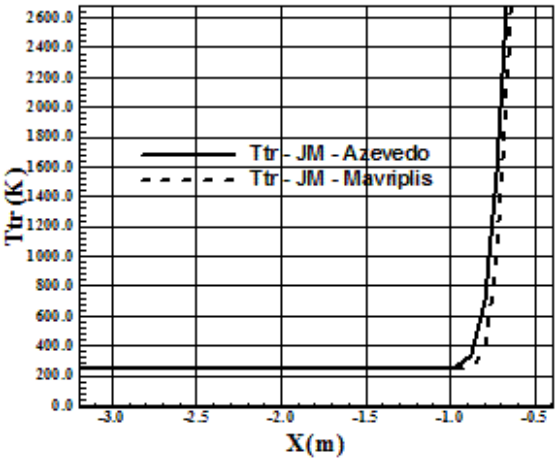

Figure 48 : Shock Position by the Temperature Profile.

Figure 48 presents the distribution of the translational / rotational temperature along the configuration symmetry line or configuration stagnation line. As can be noted, the dissipation

models predict the same shock wave positions. The [12] model predicts the shock wave at 1.00m ahead of the blunt body nose, while the [11] model predicts the shock wave at 0.90m ahead of the blunt body nose.

6.2.5 Effects over the shock wave standoff distance due to the increase of the magnetic field vector (B_y component) to the inviscid simulations in three-dimensions

To these studies, the [9] and the [10] schemes employing the artificial dissipation operator of [11], which has presented better characteristics of pressure contour severity (-Cp distributions) and shock wave standoff distance than the [12] model, were analyzed. Variations of the $B_{y,\infty}$ component between values from 0.00T (without magnetic field influence) until 0.55T, which has presented a meaningful increase in the shock standoff distance, were simulated.

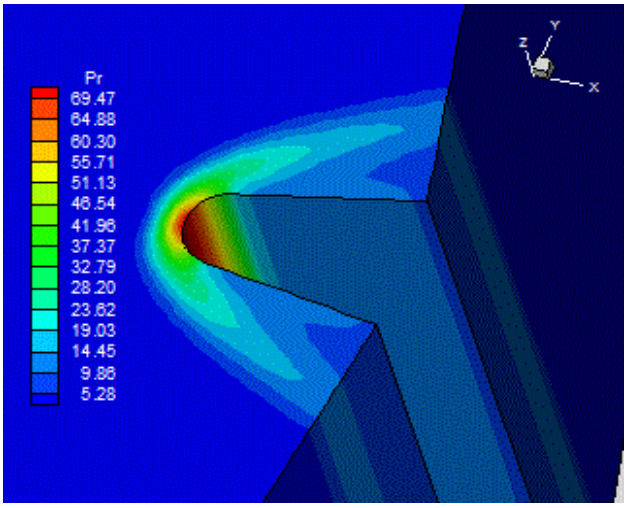

Figure 49 : Pressure Contours ($B_{y,\infty}$ = 0.00T).

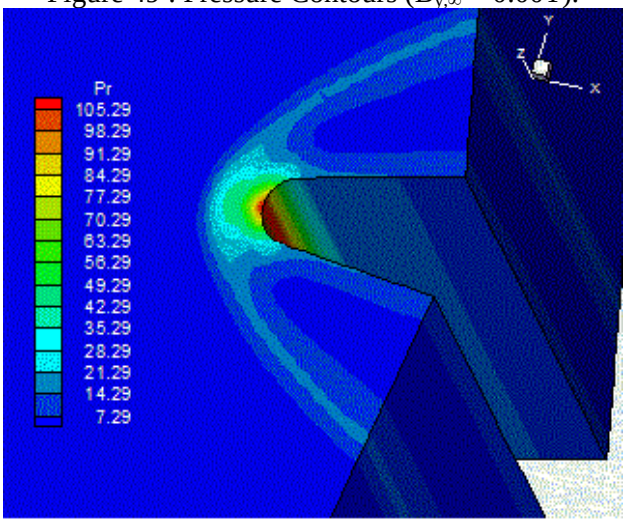

Figure 50 : Pressure Contours ($B_{y,\infty}$ = 0.55T).

Figures 49 and 50 exhibit the pressure contours around the blunt body geometry, evaluated at the computational domain, calculated by the [9] scheme with the dissipation model of [11], to the two extreme cases $B_{y,\infty}$ = 0.00T and $B_{y,\infty}$ = 0.55T. As can be observed, Fig. 49 presents the shock very close to the configuration nose. Figure 50, however, exhibits a shock wave more detached from the configuration nose, which leads to a temperature field less intense, reducing the heating from the configuration nose.

Figure 51 and 52 show the translational / rotational temperature contours around the blunt body geometry, to the two extreme cases $B_{y,\infty}$ = 0.00T and $B_{y,\infty}$ = 0.55T.

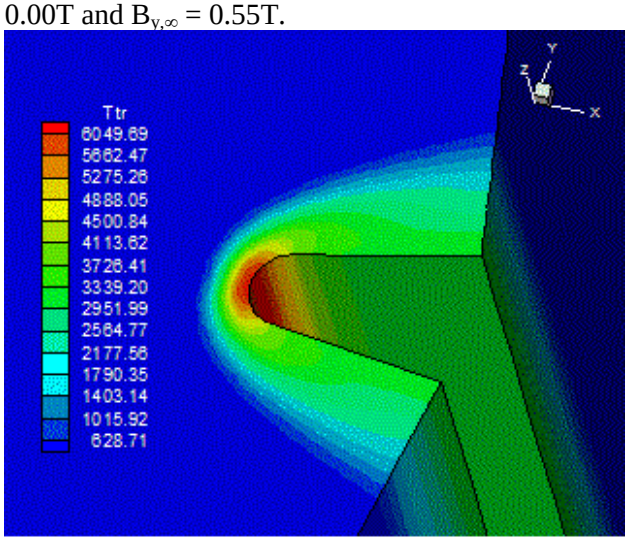

Figure 51 : Temperature Contours ($B_{y,\infty}$ = 0.00T).

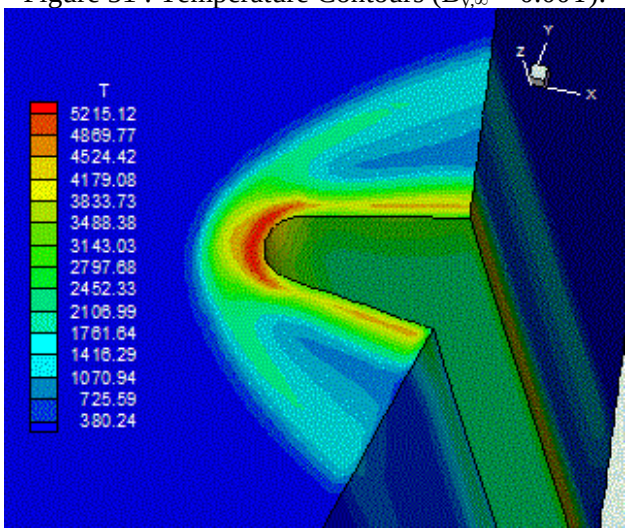

Figure 52 : Temperature Contours ($B_{y,\infty}$ = 0.55T).

As can be observed, the solution without the magnetic field presents a normal shock attached to the configuration nose, while the solution with the maximum value of $B_{y,\infty}$ presents a shock wave more detached from the blunt body nose. According to the expected behavior, the temperature peak in this last solution (with magnetic field different from zero) is smaller than the respective temperature peak of the solution without the influence of the magnetic field.

This is the expected behavior because with bigger shock standoff distance less the range of reached temperatures. Hence, the [9] scheme agrees faithfully with the results of [23-24].

Figure 53 exhibits the pressure along the stagnation line of the blunt body geometry. This distribution serves to define the shock standoff distance along the stagnation line. The graphic is plotted with the non-dimensional pressures along the stagnation line as function of the x coordinate along the symmetry line. As can be observed, as the increase of the $B_{y,\infty}$ intensity is bigger, bigger is the shock standoff distance in relation to the not influence of the magnetic field.

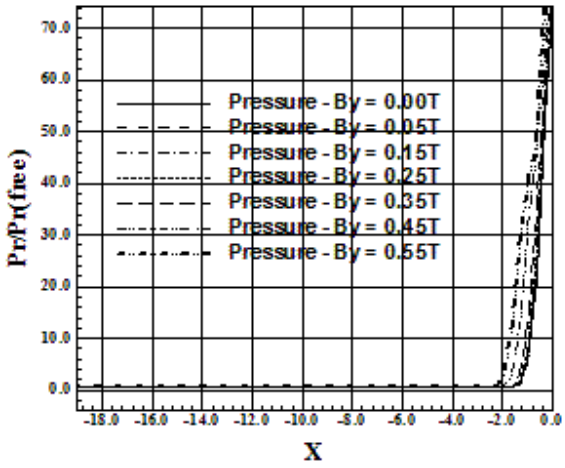

Figure 53 : Pressure Distributions at the Stagnation Line.

Table 2 exhibits the shock standoff distance to each value of the $B_{y,\infty}$ component.

Table 2 : Values of normal shock standoff distance due to variations in $B_{y,\infty}$ - [9].

$B_{y,\infty}$ (T)	X_{shock} (m)
0.00	1.9322
0.05	1.9322
0.15	1.9322
0.25	2.5763
0.35	2.2542
0.45	2.2542
0.55	2.8983

It is possible to conclude from this table that the biggest shock standoff distance occurs to the maximum studied magnetic field intensity, $B_{y,\infty}$ = 0.55T, corresponding to a distance of 2.8983m. These qualitative results accords with the literature: [23-24].

Figures 54 and 55 exhibit the pressure contours around the blunt body configuration, evaluated at the computational domain, calculated by the [10] scheme with the dissipation model of [11], to the two extreme cases $B_{y,\infty}$ = 0.00T and $B_{y,\infty}$ = 0.55T. As can be observed, Fig. 54 presents the shock attached to the blunt body nose. Figure 55 shows the shock more detached from the configuration nose, which leads to a less intense temperature field, reducing the heating at the nose.

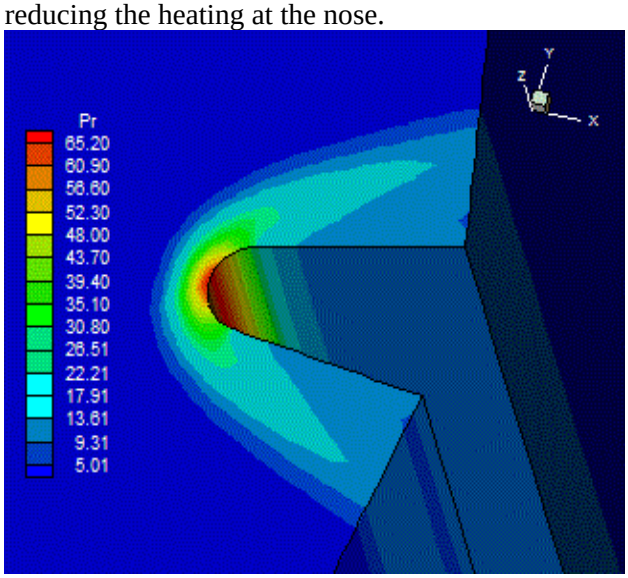

Figure 54 : Pressure Contours ($B_{y,\infty}$ = 0.00T).

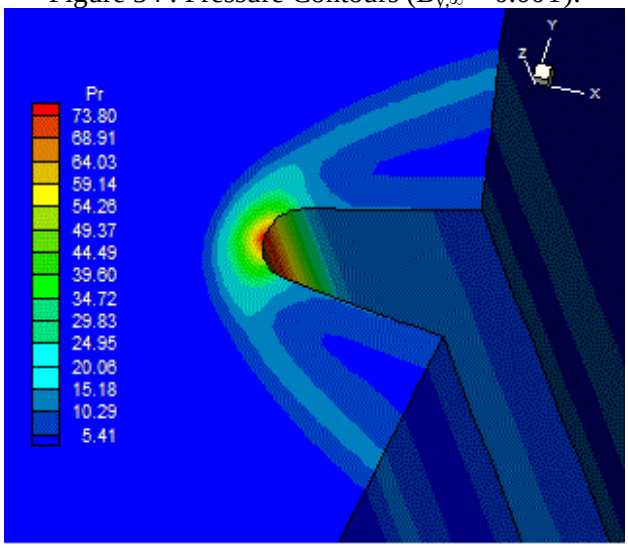

Figure 55 : Pressure Contours ($B_{y,\infty}$ = 0.55T).

Figure 56 and 57 present the translational / rotational temperature contours around the blunt body geometry. As can be observed, the solution without the influence of a magnetic field presents a normal shock attached to the configuration nose, while the solution with the maximum value of $B_{y,\infty}$ presents a shock more detached from the blunt body nose. As expected behavior, the temperature peak in the latter solution (with a magnetic field different from zero) is less than the respective temperature peak of the solution without the influence of a magnetic field, which accords with the theory

because with bigger shock standoff distance, less the temperature ranges reached by the flow. With it, the [10] scheme presents the correct evaluation of the temperature field. By this analyze, a reduction in the heating of the configuration nose as submitted to a magnetic field more intense is obtained.

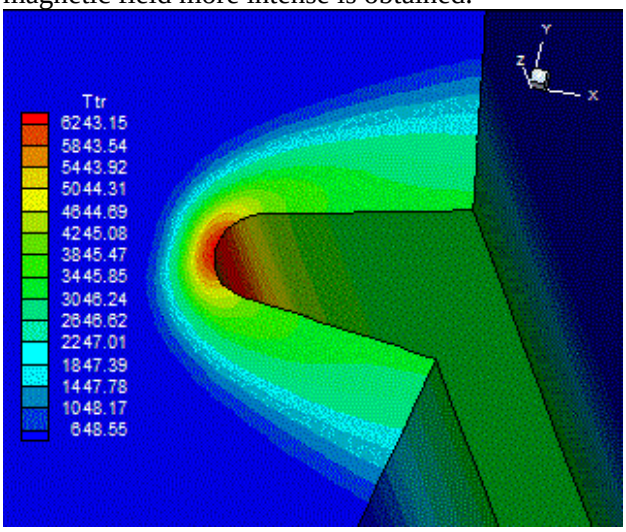

Figure 56 : Temperature Contours ($B_{y,\infty}$ = 0.00T).

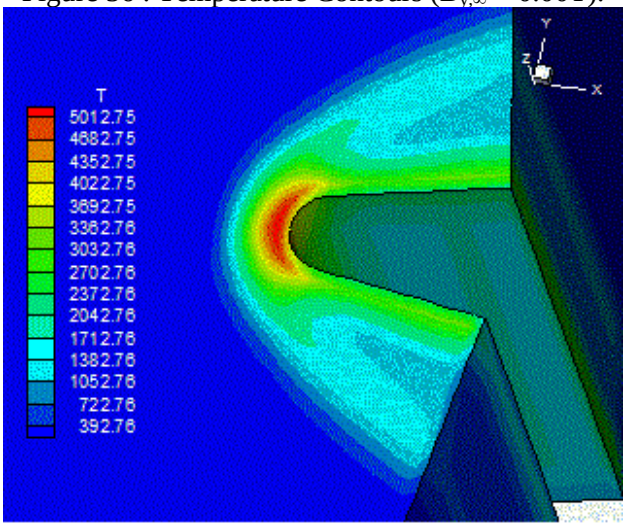

Figure 57 : Temperature Contours ($B_{y,\infty}$ = 0.55T).

Figure 58 exhibits the pressure distribution along the stagnation line of the blunt body geometry. This distribution serves to define the shock standoff distance along the stagnation line. The graphic is plotted with the non-dimensional pressures at the stagnation line as function of the x coordinate along the symmetry line. As can be observed, as the $B_{y,\infty}$ intensity increases, bigger shock standoff distance occurs in relation to the condition of flow without the magnetic field influence. Table 3 presents the shock standoff distance to each value of $B_{y,\infty}$. It is possible to conclude from this table that the biggest normal shock standoff distance occurs to the maximum studied magnetic field intensity of $B_{y,\infty}$ = 0.55T, corresponding to a distance of 2.5763m. These qualitative results accord to the literature: [23-24].

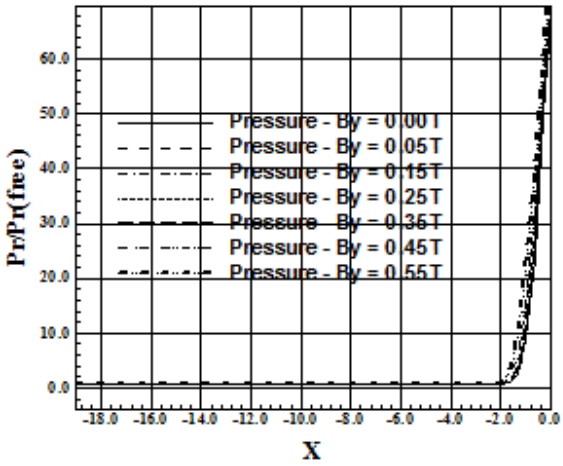

Figure 58 : Pressure Distributions at the Stagnation Line.

Table 3 : Values of the normal shock standoff distance due to variations in $B_{y,\infty}$ - [10].

$B_{y,\infty}$ (T)	X_{shock} (m)
0.00	1.9322
0.05	1.9322
0.15	2.2542
0.25	2.2542
0.35	2.2542
0.45	2.2542
0.55	2.5763

As can be observed, the [10] scheme employing the artificial dissipation model of [11] has presented the solutions more accurate and more consistent, serving as the reference algorithm to this study.

6.3 Computational performance of the studied algorithms

Table 4 presents the computational data of the simulations with magnetic field influence over a blunt body configuration in three-dimensions. The table shows the studied cases, the CFL number of the simulations, the iterations to convergence and the values of k_2 and k_4 employed in each simulation. The major cases converged in four (4) orders of reduction of the maximum residual. The distribution of the CFL number was as follows: 0.5 in two cases (25.00%), 0.3 in two cases (25.00%), 0.2 in three cases (37.50%) and 0.1 in one case (12.50%). The maximum number of iterations to convergence reached less than 30,100 iterations, with the solution of the [9] scheme employing the dissipation model of [11]. In cases in which the [10] scheme was employed, the number of iterations to convergence

was inferior to 5,000. The [9] scheme needed to employ the value of 0.75 to the k_2 coefficient (stability in presence of shock waves) in two cases to obtain convergence: viscous case with the dissipation models [11-12]. The [10] scheme needed to use the value 0.75 to k_2 coefficient in one case: viscous case with [11] dissipation model. It is important to emphasize that all viscous simulations were considered laminar, without the introduction of a turbulence model, although a raised Reynolds number was employed in the simulations.

Table 4. Computational data from the blunt body simulations.

Studied case	CFL	Iterations	k_2 / k_4
I[(1)]/[9]/[11]	0.3	1,443	0.50 / 0.01
V[(2)]/[9]/[11]	0.1	30,010	0.75 / 0.01
I/[9]/[12]	0.3	2,822	0.50 / 0.01
V/[9]/[12]	0.2	4,039	0.75 / 0.01
I/[10]/[11]	0.5	3,445	0.50 / 0.01
V/[10]/[11]	0.2	4,737	0.75 / 0.01
I/[10]/[12]	0.5	2,998	0.50 / 0.01
V/[10]/[12]	0.2	3,699	0.50 / 0.01

(1): Inviscid; (2): Viscous.

Table 5. Computational costs of the structured schemes of [9] and [10].

Studied case	Computational cost[(1)]
Inviscid/[9]/[12]	0.0004878
Viscous/[9]/[12]	0.0005889
Inviscid/[9]/[11]	0.0005217
Viscous/[9]/[11]	0.0006341
Inviscid/[10]/[12]	0.0011975
Viscous/[10]/[12]	0.0023405
Inviscid/[10]/[11]	0.0013678
Viscous/[10]/[11]	0.0025679

(1) Measured in seconds/per iteration/per computational cell.

Table 5 presents the computational costs of the [9] and of [10] schemes in the formulation which considers the influence of the magnetic field, employing the artificial dissipation models of [11] and of [12]. This cost is evaluated in seconds/per iteration/per computational cell. The costs were calculated employing a notebook with 2.13GHz of clock and 1.0GBytes of RAM, in the Windows Vista Starter environment. The cheapest algorithm was the [9] scheme, in the inviscid simulation, employing the [12] artificial dissipation model, while the most expensive was the [10] scheme, in the viscous simulation, employing the artificial dissipation model of [11]. In relative percentage terms, the former is 426.43% cheaper than the latter. The [10] algorithms are more expensive than the [9] algorithms because the former calculates the flux at interfaces by arithmetical average between the flux vectors, while the latter employ the forward or backward values in relation to the flux interface in each predictor or corrector step, respectively, dismissing the average calculations.

7 Conclusions

The present work aimed to implement a computational tool to simulation of inviscid and viscous flows employing a magnetic field formulation acting on a specific geometry. In this study, the Euler and the Navier-Stokes equations employing a finite volume formulation, following a structured spatial discretization, were solved. The aerospace problem of the hypersonic flow around a blunt body geometry was simulated. A spatially variable time step procedure was employed aiming to accelerate the convergence of the numerical schemes to the steady state solution. Effective gains in terms of convergence acceleration are observed with this technique ([13-14]).

The study with magnetic field employed the [9] and the [10] algorithms to perform the numerical experiments. The [9] scheme is calculated by forward and backward values to the convective flux vectors at the flux interface, in the predictor and corrector steps, respectively. The [10] scheme is calculated by arithmetical average between the convective flux vectors at the flux interface, opposed to the arithmetical average between the conserved variable vector. The viscous flux vectors are calculated by arithmetical average of the conserved variables and of the gradients. This procedure to the viscous simulations is employed by the [9] and by the [10] schemes. The results, mainly those obtained with the [10] algorithm, are of good quality. In particular, it was demonstrated the effect that the imposition of a normal magnetic field in relation to the symmetry line of a blunt body geometry could cause the increase of the shock standoff distance, reducing, hence, the aerodynamic heating. This effect is important and can be explored in the phases of aerospace vehicle project which does reentry in the atmosphere normal to the earth magnetic field. Another option would be the proper vehicle generates an oscillatory electrical field to yield a magnetic field in it and to induce the effect of the increase of the shock standoff distance. These are suggestions to verify.

The cheapest algorithm was the [9] scheme, in the inviscid simulation, employing the [12] dissipation model, while the most expensive was the [10] scheme, in the viscous simulation, employing

the artificial dissipation model of [11]. In relative percentage terms, the former is 426.43% cheaper than the latter. The [10] algorithms are more expensive than the [9] algorithms because the former calculates the inviscid flux at interfaces by arithmetical average between the flux vectors, while the latter employ the forward or backward values in relation to the flux interface in each predictor or corrector step, respectively, dismissing the average calculations.

8 Acknowledgments

The first author acknowledges the CNPq by the financial support conceded under the form of a DTI (Industrial Technological Development) scholarship no. 384681/2011-5. He also acknowledges the infra-structure of the ITA that allowed the realization of this work.

References:

[1] P. A. Davidson, Magnetohydrodynamics in Materials Processing, *Ann. Rev. Fluid Mech.*, Vol. 31, 1999, pp. 273-300.

[2] R. W. Ziemer, and W. B. Bush, Magnetic Field Effects on Bow Shock Stand-Off Distance, *Physical Review Letters*, Vol. 1, No. 2, 1958, pp. 58-59.

[3] R. X. Meyer, Magnetohydrodynamics and Aerodynamic Heating, *ARS Journal*, Vol. 29, No. 3, 1959, pp. 187-192.

[4] E. P. Gurijanov, and P. T. Harsha, Ajax: New Directions in Hypersonic Technology, *AIAA Paper 96-4609*, 1996.

[5] D. I. Brichkin, A. L. Kuranov, and E. G. Sheikin, MHD-Technology for Scramjet Control, *AIAA Paper 98-1642*, 1998.

[6] Y. C. Ganiev, V. P. Gordeev, A. V. Krasilnikov, V. I. Lagutin, V. N. Otmennikov, and A. V. Panasenko, Theoretical and Experimental Study of the Possibility of Reducing Aerodynamic Drag by Employing Plasma Injection, *AIAA Paper 99-0603*, 1999.

[7] I. V. Adamovich, V. V. Subramaniam, J. W. Rich, and S. O. Macheret, Phenomenological Analysis of Shock-Wave Propagation in Weakly Ionized Plasmas, *AIAA Journal*, Vol. 36, No. 5, 1998, pp. 816-822.

[8] D. V. Gaitonde, Development of a Solver for 3-D Non-Ideal Magnetogasdynamics, *AIAA Paper 99-3610*, 1999.

[9] R. W. MacCormack, The Effect of Viscosity in Hypervelocity Impact Cratering, *AIAA Paper 69-354*, 1969.

[10] A. Jameson, and D. J. Mavriplis, Finite Volume Solution of the Two-Dimensional Euler Equations on a Regular Triangular Mesh, *AIAA Journal*, Vol. 24, No. 4, 1986, pp. 611-618.

[11] D. J. Mavriplis, Accurate Multigrid Solution of the Euler Equations on Unstructutred and Adaptive Meshes, *AIAA Journal*, Vol. 28, No. 2, 1990, pp. 213-221.

[12] J. L. F. Azevedo, On the Development of Unstructured Grid Finite Volume Solvers for High Speed Flows, *NT-075-ASE-N*, IAE, CTA, São José dos Campos, SP, Brazil, 1992.

[13] E. S. G. Maciel, Analysis of Convergence Acceleration Techniques Used in Unstructured Algorithms in the Solution of Aeronautical Problems – Part I, *Proceedings of the XVIII International Congress of Mechanical Engineering (XVIII COBEM)*, Ouro Preto, MG, Brazil, 2005. [CD-ROM]

[14] E. S. G. Maciel, Analysis of Convergence Acceleration Techniques Used in Unstructured Algorithms in the Solution of Aerospace Problems – Part II, *Proceedings of the XII Brazilian Congress of Thermal Engineering and Sciences (XII ENCIT)*, Belo Horizonte, MG, Brazil, 2008. [CD-ROM]

[15] J. C. Tannehill, D. A. Anderson, and R. H. Pletcher, *Computational Fluid Mechanics and Heat Transfer*, Second Edition, Hemisphere Publishing Corporation, 792p, 1997.

[16] E. S. G. Maciel, Comparação entre Diferentes Modelos de Dissipação Artificial Aplicados a um Sistema de Coordenadas Generalizadas – Parte I, *Proceedings of the 7th Symposium of Computational Mechanics (VII SIMMEC)*, Araxá, MG, Brazil, 2006.

[17] E. S. G. Maciel, Comparison Among Different Artificial Dissipation Models Applied to a Generalized Coordinate System, *Proceedings of the 8th Symposium of Computational Mechanics (VIII SIMMEC)*, Belo Horizonte, MG, Brazil, 2008.

[18] A. Jameson, W. Schmidt, and E. Turkel, Numerical Solution for the Euler Equations by Finite Volume Methods Using Runge-Kutta Time Stepping Schemes, *AIAA Paper 81-1259*, 1981.

[19] R. C. Swanson, and R. Radespiel, Cell Centered and Cell Vertex Multigrid Schemes for the Navier-Stokes Equations, *AIAA Journal*, Vol. 29, No. 5, 1991, pp. 697-703.

[20] L. N. Long, M. M. S. Khan, and H. T. Sharp, Massively Parallel Three-Dimensional Euler / Navier-Stokes Method, *AIAA Journal*, Vol. 29, No. 5, 1991, pp. 657-666.

[21] E. S. G. Maciel, Relatório ao CNPq (Conselho Nacional de Desenvolvimento Científico e Tecnológico) sobre as atividades de pesquisa realizadas no período de 01/10/2011 até 30/09/2012 com relação ao projeto DTI número 384681/2011-5, *Report, National Council of Scientific and Technological Development (CNPq)*, São José dos Campos, SP, Brazil, 2012. (To be written)

[22] R. W. Fox, and A. T. McDonald, *Introdução à Mecânica dos Fluidos*, Editora Guanabara, 1988.

[23] H. –M. Damevin, J. –F. Dietiker, and K. A. Hoffmann, Hypersonic Flow Computation with Magnetic Field, *AIAA Paper 2000-0451*, 2000.

[24] K. A. Hoffmann, H. –M. Damevin, J. –F. Dietiker, Numerical Simulations of Hypersonic Magnetohydrodynamic Flows, *AIAA Paper 2000-2259*, 2000.